

Numerical and analytical analyses of a matrix model with non-pairwise contracted indices

Naoki Sasakura* and Shingo Takeuchi†

* *Yukawa Institute for Theoretical Physics, Kyoto University,
Kitashirakawa, Sakyo-ku, Kyoto 606-8502, Japan*

† *Phenikaa Institute for Advanced Study and Faculty of Basic Science,
Phenikaa University, Hanoi 100000, Vietnam*

March 29, 2022

Abstract

We study a matrix model that has ϕ_a^i ($a = 1, 2, \dots, N$, $i = 1, 2, \dots, R$) as its dynamical variable, whose lower indices are pairwise contracted, but upper ones are not always done so. This matrix model has a motivation from a tensor model for quantum gravity, and is also related to the physics of glasses, because it has the same form as what appears in the replica trick of the spherical p -spin model for spin glasses, though the parameter range of our interest is different. To study the dynamics, which in general depends on N and R , we perform Monte Carlo simulations and compare with some analytical computations in the leading and the next-leading orders. A transition region has been found around $R \sim N^2/2$, which matches a relation required by the consistency of the tensor model. The simulation and the analytical computations agree well outside the transition region, but not in this region, implying that some relevant configurations are not properly included by the analytical computations. With a motivation coming from the tensor model, we also study the persistent homology of the configurations generated in the simulations, and have observed its gradual change from S^1 to higher dimensional cycles with the increase of R around the transition region.

*sasakura@yukawa.kyoto-u.ac.jp

†shingo.portable@gmail.com

Contents

1	Introduction	1
2	The model	4
3	Observables	6
4	Computations of $f_{N,R,\lambda,\lambda_d}(t)$ in the leading and the next-leading orders	8
5	Saddle point analysis in the leading order	12
6	Comparison with Monte Carlo simulations	15
7	Topological structure of configurations	18
8	Summary and future prospects	22
A	$R = 2$ case	23
B	Derivation of (29)	25
C	Computation of $f_{N,R,\Lambda_{ij}}(t)$ in the next-leading order	25
D	Brief introduction of persistent homology	31

1 Introduction

Quantization of gravity is one of the major fundamental problems in theoretical physics. The quantization of general relativity by the standard perturbative methods of quantum field theory fails due to non-renormalizable divergences. Various approaches have been proposed and being studied to solve the fundamental problem, depending on views of authors. In one approach, general relativity (with higher derivative terms) is directly quantized as quantum field theory with the modern technique of the functional renormalization group [1]. In other approaches, fundamental discreteness is introduced to represent spacetimes, which include (causal) dynamical triangulations [2], loop quantum gravity [3], causal sets [4], quantum graphity [5], matrix models [6, 7, 8, 9, 10], tensor models [11, 12, 13, 14], and so on. In these discretized approaches, an important criterion for success is whether macroscopic spacetimes

are generated, or in other words, whether there exist appropriate continuum limits that recover the usual continuum picture of spacetime with dynamics described by general relativity as low-energy effective theory.

The criterion above can in principle be checked by studying the properties of a wave function of each theory. If the wave function has a peak at a configuration that can well be described by a macroscopic spacetime picture, then the model can be considered to be potentially successful. An indirect motivation for the present paper is to understand the properties of the wave function [15] that is an exact solution to a tensor model in the Hamilton formalism [16, 17]. It has been argued and shown for some simple cases that the wave function has peaks at the tensor values that are invariant under Lie groups [18]. By using the correspondence developed in [19] between tensor values and spaces with geometries, this would imply that the spacetimes symmetric under Lie groups are favored quantum mechanically. However, the main difficulty in arguing this is that only little part of the peak structure (often called landscape in such contexts) of the wave function is known, not enough to discuss “probabilities of spacetimes.”

To simplify the problem keeping the main structure from the tensor model as much as possible, one of the authors of the present paper and his collaborators considered the following two simplifications in the former papers. One is that they considered a toy wave function rather than the actual wave function of the tensor model [20]. The actual wave function is expressed by a certain power, say R -th, of a function expressed by an integration over $N + 1$ variables, but, in the toy wave function, the function is simplified to the one expressed by an integration over N variables by fixing a certain integration variable to a constant. While this substantially simplifies the analysis, the toy wave function keeps the most crucial property mentioned above that there appear peaks at the tensor values that are symmetric under Lie groups as the actual wave function of the tensor model does [20].

Though this toy wave function is simpler than the actual one, it is still difficult to perform thorough analyses, because the dimension of the argument (a symmetric tensor with three indices) of the wave function is very large with the order of $\sim N^3/6$. Therefore, as an additional simplification, the authors in [21] considered a model that can be obtained by integrating over the argument of the toy wave function. This gives a dynamical system of a matrix, say ϕ_a^i ($a = 1, 2, \dots, N$, $i = 1, 2, \dots, R$), rectangular in general, where the lower indices are pairwise contracted, but the upper ones are not always done so. While this model does not fall into the known solvable models such as the rectangular matrix models [22, 23, 24] or the vector models [25, 26], it has the same form as the one that appears when the replica trick is applied to the spherical p -spin model for spin glasses [27, 28], where R plays the role of the replica number. Here, though the form is exactly so, the concerned ranges of the dynamical variables and the parameters are different between our model and the spin glass model, and it seems reasonable to reanalyze the matrix model with fresh eyes: (i) While the replica number R is taken to vanish in the replica trick, it takes a finite value $R \sim N^2/2$ in the correspondence to the tensor model, and should rather be taken to infinity in the thermodynamic limit $N \rightarrow \infty$; (ii) A coupling constant of the model¹ takes the opposite sign in our model compared to the

¹More specifically, λ in (1).

spin glass model; (iii) There is a spherical constraint on the dynamical variable in the spherical p -spin model, but there is none in our model.

In this paper, we numerically study the matrix model by the Monte Carlo simulation with the standard Metropolis update method. This contrasts with the perturbative analytical computations performed in the previous paper [21]. We also perform some additional analytical computations to compare with the numerical results. We have obtained the following main results:

- The expectation values of some observables are computed by the numerical simulations, and it is observed that there exists a transition region around $R \sim N^2/2$. Intriguingly, the location is in good coincidence with $R = (N+2)(N+3)/2$ that is required by the consistency of the tensor model (the hermiticity of its Hamiltonian constraint) [18, 15, 29]. Presently, this coincidence is mysterious, since there are no apparent connections between the transition and the consistency. The observables seem to continuously but substantially change their behavior at the transition region, but it has not been determined whether this transition is a phase transition or a crossover. The method for the Monte Carlo simulations performed in this paper is not powerful enough for the determination because of an issue explained below.
- The expectation values of some observables are analytically computed in the leading order, mostly based on the treatment in the previous paper [21], and are compared with the numerical results. Good agreement between them is obtained outside the vicinity of the transition region, while there exist deviations in the transition region. The deviations are such that they soften the transition to make it look more like a crossover. A next-leading order computation has also been performed, but this does not well correct the deviations.
- The tensor model suggests the presence of topological characteristics for the dominant configurations of the matrix ϕ_a^i . Therefore, we have studied topological characters of the configurations that are generated in the simulations by using the modern technique called persistent homology [30] in the topological data analysis. This technique extracts homology groups possessed by a data, which is a value of the matrix ϕ_a^i in our case. The favored topology gradually changes from S^1 to higher-dimensional cycles with the increase of R in the vicinity of the transition region.
- The Monte Carlo simulation becomes substantially difficult in the region with $R \gtrsim N^2/2$ and large λ/k^3 , where λ and k are the parameters of our model (1). In the region, the step sizes of the Metropolis updates chosen for reasonable acceptance rates become too small to reach thermal equilibriums in $\sim 10^{10}$ Metropolis updates.
- A characterization of the transition can be done by the sizes of the matrix components, which take relatively large values at the region with $R \gtrsim N^2/2$ and large λ/k^3 , but otherwise fluctuate around small values. In the former case, our model may behave like the spherical p -spin model, since the matrix components are effectively constrained to non-zero sizes, which would approximately realize the spherical constraint in the

spherical p -spin model. This may partly explain the bad performance of the Monte Carlo simulation in the region, because of the viscous nature of glasses.

This paper is organized as follows. In Section 2, we define the model and summarize the previous results [21] that are relevant to the present paper. In Section 3, some observables are introduced and the analytical expressions of the expectation values are obtained in a leading order. In Section 4, the details of the computation in the leading order are given. The result of the next-leading order is also presented, while the details of the computation are given in Appendix C. In Section 5, we perform a saddle point analysis of the expectation values of the observables in the leading order. This describes the transition as a continuous phase transition in the large N limit, where the first derivatives of the expectation values of the observables with respect to R are discontinuous. In Section 6, we compare the Monte Carlo and the analytical results. They agree well outside the transition region. But, in the transition region, there exist deviations, which smoothen the transition to make it look more like a crossover. In Section 7, we analyze the homology structure of the configurations generated by the simulations. The preference changes from S^1 to higher-dimensional cycles with the increase of R in the vicinity of the transition region. The last section is devoted to a summary and future prospects. In Appendix A, an instructive computation of the partition function for $R = 2$ is given. In Appendix B, a formula used in the main text is shown. In Appendix D, a brief introduction to persistent homology is given.

2 The model

The partition function of our matrix model is given by

$$Z_{N,R}(\lambda, k) := \int_{\mathbb{R}^{NR}} d\phi \exp \left(-\lambda U(\phi) - k \text{Tr}(\phi^t \phi) \right), \quad (1)$$

where λ and k are the coupling constants assumed to be positive, ϕ is a (generally rectangular) real matrix, ϕ_a^i ($a = 1, 2, \dots, N$, $i = 1, 2, \dots, R$), and $d\phi := \prod_{a=1, i=1}^{N,R} d\phi_a^i$. The integration is over the NR -dimensional real space denoted by \mathbb{R}^{NR} . The coupling terms are defined by

$$\begin{aligned} U(\phi) &:= \sum_{i,j=1}^R \left(\phi_a^i \phi_a^j \right)^3, \\ \text{Tr}(\phi^t \phi) &:= \sum_{i=1}^R \phi_a^i \phi_a^i, \end{aligned} \quad (2)$$

where the repeated lower indices are assumed to be summed over. We use this standard convention for the lower indices throughout this paper, unless otherwise stated. On the other hand, we do not use this convention for the upper indices: A sum over them must always be written explicitly.

In (2), the lower indices are contracted pairwise, while the upper indices are not necessarily so. Therefore the model has the symmetry of the $O(N)$ -rotation on the lower indices, but

only the permutation symmetry S_R of relabeling $\{1, 2, \dots, R\}$ on the upper indices. These symmetries are not enough to diagonalize ϕ_a^i in general, and therefore this model cannot be solved as the usual matrix model.

In the previous paper [21], we considered an expression which can just be obtained by separating the radial and angular part of the integration in (1): By the change of variable, $\phi_a^i = r \tilde{\phi}_a^i$, with $r^2 = \sum_{i=1}^R \phi_a^i \phi_a^i$ and $\tilde{\phi}$ representing the angular coordinates, we obtain

$$Z_{N,R}(\lambda, k) := V_{NR-1} \int_0^\infty dr r^{NR-1} f_{N,R}(\lambda r^6) e^{-k r^2}, \quad (3)$$

where

$$f_{N,R}(t) := \frac{1}{V_{NR-1}} \int_{S^{NR-1}} d\tilde{\phi} e^{-t U(\tilde{\phi})} \quad (4)$$

with $V_{NR-1} = \int_{S^{NR-1}} d\tilde{\phi}$, the volume of the $NR - 1$ -dimensional unit sphere.

This rather trivial change of expression is actually very useful, because $f_{N,R}(t)$ can be shown to be an entire function of t and therefore has a Taylor expansion in t with the infinite convergence radius around $t = 0$ (actually anywhere with $t \neq \infty$). Therefore, in principle, the dynamics can be solved by obtaining the entire perturbative series of $f_{N,R}(t)$. Note that the corresponding perturbative expansion of $Z_{N,R}(\lambda, k)$ in λ around $\lambda = 0$, often obtained by perturbative methods, is merely an asymptotic series, because $Z_{N,R}(\lambda, k)$ has an essential singularity at $\lambda = 0$. The $f_{N,R}(t)$ has also the property that it is a decreasing positive function of t with $f_{N,R}(0) = 1$ for real t . This property provides a good criterion for assessing the validity of an approximation of $f_{N,R}(t)$. In the previous paper [21], $f_{N,R}(t)$ in the leading order of $1/R$ has been determined by a Feynman diagrammatic method with the result,

$$f_{N,R}^{1/R, \text{leading}}(t) := \left(1 + \frac{12t}{N^3 R^2}\right)^{-\frac{N(N-1)(N+4)}{12}} \left(1 + \frac{6(N+4)t}{N^3 R^2}\right)^{-\frac{N}{2}}. \quad (5)$$

In particular, (5) indeed satisfies the properties above: It is decreasing in t and is almost an entire function, since the locations of the poles are far away from the relevant region $t \geq 0$ for large N, R .

Since there are two parameters N, R , which can be taken large, the range of validity of (5), which was derived in the leading order of $1/R$, is not obvious. However, in later sections, we will find that (5)² will give results which agree well³ with those of the numerical simulations except for the transition region around $R \sim N^2/2$.

²More precisely, because of the difference of our strategy of computations taken in this paper, the expression (17) is slightly different from (5) obtained in [21]. However, the difference is negligible for large N, R , and is not essential.

³In fact, the expression (5) cannot be correct for small R such as $R = 2$. This is explicitly shown in Appendix A. However, the difference shown there in the asymptotic region $t \sim \infty$ is not relevant for the thermodynamic properties, since for small R , the dominant contributions come from $t \sim 0$.

3 Observables

The purpose of this section is to introduce some observables, say $\mathcal{O}(\phi)$, and discuss the expectation values defined by

$$\langle \mathcal{O}(\phi) \rangle := \frac{1}{Z_{N,R}(\lambda, k)} \int_{\mathbb{R}^{NR}} d\phi \mathcal{O}(\phi) \exp(-\lambda U(\phi) - k \text{Tr}(\phi^t \phi)). \quad (6)$$

The observables must respect the symmetry $O(N) \times S_R$ mentioned in Section 2. Among various possibilities, we consider $\text{Tr}(\phi^t \phi)$ and $U(\phi)$ in (2), and also

$$U_d(\phi) := \sum_{i=1}^R (\phi_a^i \phi_a^i)^3. \quad (7)$$

The last one is the diagonal part of the sum in $U(\phi)$ in (2). Since these observables are some parts contained in the exponent of (1), they can be implemented in the numerical simulations with little additional computational costs.

To compute the expectation values of these observables, it is convenient to extend (1) by introducing the coupling constant λ_d conjugate to $U_d(\phi)$ as

$$Z_{N,R}(\lambda, \lambda_d, k) := \int_{\mathbb{R}^{NR}} d\phi \exp(-\lambda U(\phi) - \lambda_d U_d(\phi) - k \text{Tr}(\phi^t \phi)). \quad (8)$$

Then the expectation values can respectively be expressed as

$$\begin{aligned} \langle \text{Tr}(\phi^t \phi) \rangle &= \frac{\partial}{\partial k} F_{N,R}(\lambda, \lambda_d = 0, k), \\ \langle U(\phi) \rangle &= \frac{\partial}{\partial \lambda} F_{N,R}(\lambda, \lambda_d = 0, k), \\ \langle U_d(\phi) \rangle &= \left. \frac{\partial}{\partial \lambda_d} F_{N,R}(\lambda, \lambda_d, k) \right|_{\lambda_d=0}, \end{aligned} \quad (9)$$

where $F_{N,R}(\lambda, \lambda_d, k) := -\log Z_{N,R}(\lambda, \lambda_d, k)$, which is the free energy of the model. Here we have put $\lambda_d = 0$ at last, since our interest is in (1) corresponding to $\lambda_d = 0$ of (8).

To compute the partition function (8), it is convenient to first separate the radial and the angular part as in (3):

$$Z_{N,R}(\lambda, \lambda_d, k) = V_{NR-1} \int_0^\infty dr r^{NR-1} f_{N,R,\lambda,\lambda_d}(r^6) e^{-kr^2}, \quad (10)$$

where

$$f_{N,R,\lambda,\lambda_d}(t) := \frac{1}{V_{NR-1}} \int_{S^{NR-1}} d\tilde{\phi} \exp(-\lambda t U(\tilde{\phi}) - \lambda_d t U_d(\tilde{\phi})). \quad (11)$$

The $f_{N,R,\lambda,\lambda_d}(t)$ has the similar properties as $f_{N,R}(t)$ explained in Section 2: It is an entire function of t ; For $\lambda, \lambda_d > 0$, it is positive and decreasing in t for real t ; $f_{N,R,\lambda,\lambda_d}(0) = 1$. With $f_{N,R,\lambda,\lambda_d}(t)$, the observables (9) can be expressed by

$$\begin{aligned}\langle \text{Tr}(\phi^t \phi) \rangle &= \frac{1}{\mathcal{N}_f} \int_0^\infty dr \, r^{NR+1} f_{N,R,\lambda,0}(r^6) e^{-kr^2}, \\ \langle U(\phi) \rangle &= -\frac{1}{\mathcal{N}_f} \int_0^\infty dr \, r^{NR-1} \frac{\partial}{\partial \lambda} f_{N,R,\lambda,0}(r^6) e^{-kr^2}, \\ \langle U_d(\phi) \rangle &= -\frac{1}{\mathcal{N}_f} \int_0^\infty dr \, r^{NR-1} \frac{\partial}{\partial \lambda_d} f_{N,R,\lambda,\lambda_d}(r^6) \Big|_{\lambda_d=0} e^{-kr^2},\end{aligned}\tag{12}$$

where the normalization is given by

$$\mathcal{N}_f = \int_0^\infty dr \, r^{NR-1} f_{N,R,\lambda,0}(r^6) e^{-kr^2}.\tag{13}$$

From the leading order computation, which is detailed in Section 4, we obtain

$$f_{N,R,\lambda,\lambda_d}^{\text{leading}}(t) = h_{N,R}(\lambda R t + \lambda_d t) h_{N,R}(\lambda_d t)^{R-1}\tag{14}$$

with

$$h_{N,R}(x) := (1 + 12\gamma_3 x)^{-\frac{N(N-1)(N+4)}{12}} (1 + 6(N+4)\gamma_3 x)^{-\frac{N}{2}},\tag{15}$$

where

$$\gamma_n := \frac{\Gamma\left(\frac{NR}{2}\right)}{2^n \Gamma\left(\frac{NR}{2} + n\right)}.\tag{16}$$

When $\lambda_d = 0$ is taken, (14) becomes

$$f_{N,R,\lambda,0}^{\text{leading}}(t) = (1 + 12\gamma_3 \lambda R t)^{-\frac{N(N-1)(N+4)}{12}} (1 + 6(N+4)\gamma_3 \lambda R t)^{-\frac{N}{2}}.\tag{17}$$

This is expected to agree with (5), but there is a slight difference coming from (16) with $n = 3$. This difference originates from the fact that the strategy of the computation we take in Section 4 is different from the one taken previously in [21], and therefore the expressions of the leading orders are slightly different from each other. However, they agree with each other in the leading order of $1/R$, since $\gamma_n \sim (NR)^{-n}$ for $NR \gg n$, as expected.

By putting these expressions into (12), we obtain

$$\begin{aligned}\langle \text{Tr}(\phi^t \phi) \rangle_{\text{leading}} &= \frac{1}{\mathcal{N}_f} \int_0^\infty dr \, r^{NR+1} f_{N,R,\lambda,0}^{\text{leading}}(r^6) e^{-kr^2}, \\ \langle U(\phi) \rangle_{\text{leading}} &= -\frac{R}{\mathcal{N}_f} \int_0^\infty dr \, r^{NR+5} \frac{h'_{N,R}(\lambda R r^6)}{h_{N,R}(\lambda R r^6)} f_{N,R,\lambda,0}^{\text{leading}}(r^6) e^{-kr^2}, \\ \langle U_d(\phi) \rangle_{\text{leading}} &= -\frac{1}{\mathcal{N}_f} \int_0^\infty dr \, r^{NR+5} \left(\frac{h'_{N,R}(\lambda R r^6)}{h_{N,R}(\lambda R r^6)} + (R-1) \frac{h'_{N,R}(0)}{h_{N,R}(0)} \right) f_{N,R,\lambda,0}^{\text{leading}}(r^6) e^{-kr^2},\end{aligned}\tag{18}$$

where \mathcal{N}_f is given by (13) with $f_{N,R,\lambda,0}^{\text{leading}}(t)$. The actual values of these integrations can be obtained numerically.

4 Computations of $f_{N,R,\lambda,\lambda_d}(t)$ in the leading and the next-leading orders

In this section, we will compute $f_{N,R,\lambda,\lambda_d}(t)$ in the leading order of t , and will also show the result in the next-leading order, whose detailed computations are given in Appendix C. In [21], the computation in the leading order of $1/R$ has been performed by using the Feynman diagrams for the ϕ_a^i variables. In this paper, however, we will take a different strategy. This is because the new strategy makes more transparent the rather complicated counting of combinatorics performed in [21], and make it straightforward to include the extra coupling $\lambda_d U_d(\phi)$ and also to consider the next order in t . For $\lambda_d = 0$, the new strategy gives essentially the same result as [21] in the leading order, as commented below (17).

Let us define

$$f_{N,R,\Lambda_{ij}}(t) := \frac{1}{V_{NR-1}} \int_{S^{NR-1}} d\tilde{\phi} e^{-t U_{\Lambda_{ij}}(\tilde{\phi})}, \quad (19)$$

where

$$U_{\Lambda_{ij}}(\tilde{\phi}) := \sum_{i,j=1}^R \Lambda_{ij} \left(\tilde{\phi}_a^i \tilde{\phi}_a^j \right)^3 \quad (20)$$

with a real symmetric matrix Λ_{ij} . The eigenvalues of the matrix Λ_{ij} are assumed to be non-negative for the convergence of the corresponding partition function. The $f_{N,R,\Lambda_{ij}}(t)$ also has the same nice properties as $f_{N,R}(t)$ that it is an entire function, which has a Taylor series expansion in t with the infinite convergence radius around $t = 0$, and is a decreasing positive function of t for real t and $\Lambda \neq 0$ with $f_{N,R,\Lambda_{ij}}(0) = 1$. If we take $\Lambda_{ij} = \lambda + \lambda_d \delta_{ij}$, (19) gives $f_{N,R,\lambda,\lambda_d}(t)$ in (11). By introducing a new variable P_{abc}^i ($a, b, c = 1, 2, \dots, N$, $i = 1, 2, \dots, R$), which is symmetric for the lower indices, one can rewrite (19) as

$$\begin{aligned} & f_{N,R,\Lambda_{ij}}(t) \\ &= \text{const.} \int_{S^{NR-1}} d\tilde{\phi} \int_{-\infty}^{\infty} \prod_{i=1}^R \prod_{a \leq b \leq c=1}^N dP_{abc}^i \exp \left(- \sum_{i=1}^R P_{abc}^i P_{abc}^i + 2I\sqrt{t} \sum_{i,j=1}^R \tilde{\Lambda}_{ij} P_{abc}^i \tilde{\phi}_a^j \tilde{\phi}_b^j \tilde{\phi}_c^j \right), \end{aligned} \quad (21)$$

where I is the imaginary unit and $\tilde{\Lambda}_{ij}$ is a symmetric matrix satisfying⁴,

$$\Lambda_{ij} = \sum_{k=1}^R \tilde{\Lambda}_{ik} \tilde{\Lambda}_{kj}. \quad (22)$$

The constant prefactor in (21) can be determined by $f_{N,R,\Lambda_{ij}}(0) = 1$.

⁴In general, such a matrix $\tilde{\Lambda}$ can be obtained as $\tilde{\Lambda} = M^t \sqrt{D} M$ by diagonalizing the matrix Λ as $\Lambda = M^t D M$ with a diagonal matrix D and an orthogonal one M .

To compute (21), let us first integrate over $\tilde{\phi}$. This change of the order of the integrations can be done, because the integration over P_{abc} with the infinite integration region converges uniformly for any $\tilde{\phi} \in S^{NR-1}$. Then our task is to compute

$$\left\langle \exp \left(2I\sqrt{t}P\tilde{\phi}^3 \right) \right\rangle_{\tilde{\phi}} = \frac{1}{V_{NR-1}} \int_{S^{NR-1}} d\tilde{\phi} \exp \left(2I\sqrt{t}P\tilde{\phi}^3 \right), \quad (23)$$

where we have used a short-hand notation,

$$P\tilde{\phi}^3 := \sum_{i,j=1}^R \tilde{\Lambda}_{ij} P_{abc}^i \tilde{\phi}_a^j \tilde{\phi}_b^j \tilde{\phi}_c^j, \quad (24)$$

and $\langle \cdot \rangle_{\tilde{\phi}}$ denotes the expectation value for the uniform probability distribution on the unit sphere S^{NR-1} .

For further computations, let us introduce the cumulants $\langle \mathcal{O}^n \rangle^c$ defined by⁵

$$\log \langle e^{s\mathcal{O}} \rangle = \sum_{n=1}^{\infty} \frac{s^n}{n!} \langle \mathcal{O}^n \rangle^c \quad (25)$$

for arbitrary s . Then (21) can be rewritten as

$$f_{N,R,\Lambda_{ij}}(t) = \text{const.} \int_{-\infty}^{\infty} \prod_{i=1}^R \prod_{a \leq b \leq c=1}^N dP_{abc}^i e^{-S_{eff}(P)} \quad (26)$$

with

$$S_{eff}(P) = \sum_{i=1}^R P_{abc}^i P_{abc}^i - \sum_{n=1}^{\infty} \frac{(2I\sqrt{t})^n}{n!} \langle (P\tilde{\phi}^3)^n \rangle_{\tilde{\phi}}^c, \quad (27)$$

where $S_{eff}(P)$ can be regarded as an effective action of P_{abc}^i after integrating out $\tilde{\phi}$, and it is given in terms of the perturbative expansion in t . Due to the form (24), the n -th order cumulant gives the n -th order interaction term of P_{abc}^i , and all the terms with odd n vanish because of the obvious invariance of the integration over $\tilde{\phi}$ under $\tilde{\phi} \rightarrow -\tilde{\phi}$.

Let us compute the quadratic term with $n = 2$ in (27). Since $\langle P\tilde{\phi}^3 \rangle_{\tilde{\phi}} = 0$, we obtain

$$\langle (P\tilde{\phi}^3)^2 \rangle_{\tilde{\phi}}^c = \langle (P\tilde{\phi}^3)^2 \rangle_{\tilde{\phi}} = \sum_{i,j,i',j'=1}^R \tilde{\Lambda}_{ij} \tilde{\Lambda}_{i'j'} P_{abc}^i P_{a'b'c'}^{i'} \langle \tilde{\phi}_a^j \tilde{\phi}_b^j \tilde{\phi}_c^j \tilde{\phi}_{a'}^{j'} \tilde{\phi}_{b'}^{j'} \tilde{\phi}_{c'}^{j'} \rangle_{\tilde{\phi}} \quad (28)$$

⁵Cumulants are more familiar as connected correlation functions in particle physics, because they can be computed by summing over connected Feynman diagrams. However, we do not use this terminology here, because we will rewrite the cumulants for $\tilde{\phi}$ in terms of ϕ as in (29), and one can explicitly see that these cumulants contain some disconnected diagrams in terms of the Feynman diagrams of ϕ in general, because of the extra factor $\gamma_{m/2}$ in (29).

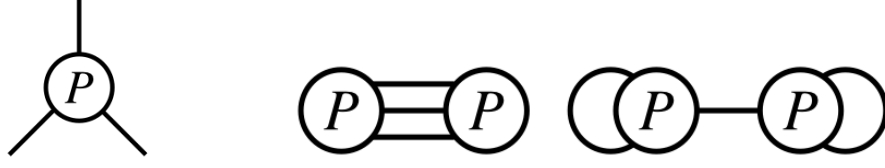


Figure 1: Left: The diagram for the interaction vertex $\sum_{i,j=1}^R \tilde{\Lambda}_{ij} P_{abc}^i \phi_a^j \phi_b^j \phi_c^j$. Right: The diagrams obtained by evaluating (28) through (29).

The integral over $\tilde{\phi}$ on S^{NR-1} , which is a curved compact space, is not easy to handle, so we use a formula which maps this integration to the Gaussian integral:

$$\langle \tilde{\phi}_{a_1}^{i_1} \tilde{\phi}_{a_2}^{i_2} \cdots \tilde{\phi}_{a_m}^{i_m} \rangle_{\tilde{\phi}} = (2\beta)^{\frac{m}{2}} \gamma_{\frac{m}{2}} \langle \phi_{a_1}^{i_1} \phi_{a_2}^{i_2} \cdots \phi_{a_m}^{i_m} \rangle_{\phi}, \quad (29)$$

where γ_n is defined in (16), and

$$\langle \phi_{a_1}^{i_1} \phi_{a_2}^{i_2} \cdots \phi_{a_m}^{i_m} \rangle_{\phi} := \frac{1}{\int_{\mathbb{R}^{NR}} d\phi e^{-\beta \text{Tr} \phi^t \phi}} \int_{\mathbb{R}^{NR}} d\phi \phi_{a_1}^{i_1} \phi_{a_2}^{i_2} \cdots \phi_{a_m}^{i_m} e^{-\beta \text{Tr} \phi^t \phi}. \quad (30)$$

Here β is a sort of dummy variable, which can be chosen freely with $\beta > 0$, and does not appear in the final expressions. In fact, as shown below, the factor $(2\beta)^{\frac{m}{2}}$ in (29) is exactly canceled by the factor in the Wick contraction (31). This formula was previously used in [21], and is proven in Appendix B so that the present paper be self-contained.

Through the replacement of (29), (28) can be computed by the standard procedure using the Wick theorem and Feynman diagrams. A Wick contraction is performed by

$$\langle \phi_a^i \phi_b^j \rangle_{\phi} = \frac{1}{2\beta} \delta_{ab} \delta^{ij}, \quad (31)$$

which can be derived from (30). The Feynman diagram for the vertex $\sum_{i,j=1}^R \tilde{\Lambda}_{ij} P_{abc}^i \phi_a^j \phi_b^j \phi_c^j$ is shown in the left figure of Figure 1. Each leg is supposed to bring the two indices of ϕ_a^i , and a Wick contraction connects two legs with the identification of their indices as in (31). A caution is that each leg on one vertex brings independent lower indices, but a common upper index.

Now let us apply the Wick contractions to what is obtained by replacing (28) with (29). We find the two diagrams shown in the right figure of Figure 1. Their degeneracy factors are 6 and 9, respectively, by counting the numbers of the ways to connect the legs of the two vertices. Since j and j' in (28) are identified by the Wick contractions, we also get $\sum_{j=1}^R \tilde{\Lambda}_{ij} \tilde{\Lambda}_{i'j} = \Lambda_{ii'}$ as a factor (See (22).). Thus, we obtain

$$\langle (P\tilde{\phi}^3)^2 \rangle_{\tilde{\phi}}^c = \gamma_3 \sum_{i,j=1}^R \Lambda_{ij} (6P_{abc}^i P_{abc}^j + 9P_{aab}^i P_{bcc}^j), \quad (32)$$

where one notices that the factor $(2\beta)^3$ coming from the replacement (29) is exactly canceled by the factors of the three Wick contractions (31) performed for the evaluation. Putting the result (32) into (27), one obtains the effective action in the second order of P_{abc}^i as

$$S_{eff}^{(2)}(P) = \sum_{i,j=1}^R (\delta_{ij} P_{abc}^i P_{abc}^j + 2\gamma_3 \Lambda_{ij} t (6P_{abc}^i P_{abc}^j + 9P_{aab}^i P_{bcc}^j)). \quad (33)$$

The computation of (26) has now been reduced to diagonalizing the quadratic expression (33). The upper and lower indices can independently be diagonalized, because (33) has the form of the direct product with respect to these indices. More explicitly, since Λ_{ij} is real symmetric, we can consider the following decomposition into the eigenspaces:

$$\Lambda_{ij} = \sum_{\lambda_{ev}} \lambda_{ev} v_i^{\lambda_{ev}} v_j^{\lambda_{ev}}, \quad (34)$$

where $v^{\lambda_{ev}}$ are the orthonormal eigenvectors, and the sum is over all the eigenvalues (with the degeneracies). By putting this and $\sum_{\lambda_{ev}} v_i^{\lambda_{ev}} v_j^{\lambda_{ev}} = \delta_{ij}$ into (33), we obtain a decomposition,

$$S_{eff}^{(2)}(P) = \sum_{\lambda_{ev}} (P_{abc}^{\lambda_{ev}} P_{abc}^{\lambda_{ev}} + 2\gamma_3 \lambda_{ev} t (6P_{abc}^{\lambda_{ev}} P_{abc}^{\lambda_{ev}} + 9P_{aab}^{\lambda_{ev}} P_{bcc}^{\lambda_{ev}})), \quad (35)$$

where $P_{abc}^{\lambda_{ev}} := v_i^{\lambda_{ev}} P_{abc}^i$.

Next let us diagonalize the lower index part in (35),

$$P_{abc} P_{abc} + 2\gamma_3 \lambda_{ev} t (6P_{abc} P_{abc} + 9P_{aab} P_{bcc}), \quad (36)$$

where for brevity we omit λ_{ev} from $P_{abc}^{\lambda_{ev}}$. Let us separate P_{abc} into the tensor part P_{abc}^T and the vector part P_{abc}^V , which are defined by⁶

$$\begin{aligned} P_{abc} &= P_{abc}^T + P_{abc}^V, \\ P_{abc}^V &= \frac{1}{N+2} (P_{add} \delta_{bc} + P_{bdd} \delta_{ca} + P_{cdd} \delta_{ab}). \end{aligned} \quad (37)$$

It is easy to check that $P_{abc}^T P_{abc}^V = 0$ and $P_{abc}^V P_{abc}^V = \frac{3}{N+2} P_{abb} P_{acc}$. In particular, the former identity implies that P_{abc}^T and P_{abc}^V are independent degrees of freedom. Then, by using (37) and these identities, (36) can be expressed as

$$(1 + 12\gamma_3 \lambda_{ev} t) P_{abc}^T P_{abc}^T + (1 + 6(N+4)\gamma_3 \lambda_{ev} t) P_{abc}^V P_{abc}^V. \quad (38)$$

The number of independent components contained in P_{abc}^T and P_{abc}^V are $\#P^T = N(N+1)(N+2)/6 - N = N(N+4)(N-1)/6$ and $\#P^V = N$, respectively. Therefore, by putting this

⁶This decomposition can be understood as follows. First P_{abb} represents the $O(N)$ -vector part of P_{abc} . Its embedding to P_{abc} is given by an expression proportional to (37). Then the coefficient can be determined by the condition that P_{abc}^T does not contain the vector part: $P_{abb}^T = 0$.

diagonal form into (26) and integrating over P^V and P^T , we finally obtain the expression of $f_{N,R,\Lambda_{ij}}(t)$ for the quadratic order as

$$\begin{aligned} f_{N,R,\Lambda_{ij}}^{(2)}(t) &= \text{const.} \int dP e^{-S_{eff}^{(2)}(P)} \\ &= \prod_{\lambda_{ev}} (1 + 12\gamma_3 \lambda_{ev} t)^{-\frac{N(N+4)(N-1)}{6}} (1 + 6(N+4)\gamma_3 \lambda_{ev} t)^{-\frac{N}{2}} \\ &= \prod_{\lambda_{ev}} h_{N,R}(\lambda_{ev} t), \end{aligned} \quad (39)$$

where we have determined the overall factor by requiring $f_{N,R,\Lambda_{ij}}^{(2)}(0) = 1$, the product is over all the eigenvalues of the matrix Λ_{ij} , and $h_{N,R}(x)$ is defined in (15).

For the computation of the observables discussed in Section 3, we consider $\Lambda_{ij} = \lambda + \lambda_d \delta_{ij}$. In this case, the matrix Λ_{ij} has one eigenvalue $\lambda R + \lambda_d$ with the eigenvector $(1, 1, \dots, 1)$, and the eigenvalue λ_d with degeneracy $R - 1$ with any of the vectors transverse to $(1, 1, \dots, 1)$ as the eigenvectors. Therefore, from (39), we obtain

$$f_{N,R,\lambda+\lambda_d\delta_{ij}}^{(2)}(t) = h_{N,R}(\lambda R t + \lambda_d t) h_{N,R}(\lambda_d t)^{R-1}. \quad (40)$$

Since this is the leading order in our treatment, we obtain (14).

As we will see later in Section 6, there are some deviations between the leading-order results above and those from the numerical simulations. To see how the situation changes by adding some corrections, we have also computed the next-leading order. The details of the computation are given in Appendix C. The final result is

$$f_{N,R,\lambda,\lambda_d}^{next-leading}(t) = f_{N,R,\lambda,\lambda_d}^{leading}(t) \left(1 - \langle S_{eff}^{(4)}(P) \rangle_P \right), \quad (41)$$

where $f_{N,R,\lambda,\lambda_d}^{next-leading}(t)$ is the sum of the leading and the next-leading orders, and

$$\begin{aligned} \langle S_{eff}^{(4)}(P) \rangle_P &= -\frac{4t^2}{4!} \left[\gamma_6 R G_1(x_1, y_1) \right. \\ &\quad \left. - 3(\gamma_3^2 - \gamma_6) (G_2(x_2, y_2) + (\lambda R + \lambda_d)^2 G_3(x_3, y_3) + (R - 1)\lambda_d^2 G_3(x_4, y_4)) \right] \end{aligned} \quad (42)$$

with the definitions of G_i, x_i, y_i given by (87) to (97).

5 Saddle point analysis in the leading order

The integral expressions of the observables (18) in the leading order do not seem to have explicit expressions with known functions. Therefore, one way to study them is to perform numerical integrations for each value of the parameters. Another way is to apply the saddle

point approximation to the integrals, which will be performed in this section. This will give a simple global picture of the phase structure of the model.

Let us recall the expression of the free energy, $F_{N,R}(\lambda, k) = -\log Z_{N,R}(\lambda, k)$, with

$$Z_{N,R}(\lambda, k) = V_{NR-1} \int_0^\infty dr r^{NR-1} f_{N,R}(\lambda r^6) e^{-kr^2}. \quad (43)$$

In the saddle point approximation, the free energy is given by

$$F_{N,R}^{saddle}(\lambda, k) = F_{N,R}(\lambda, k, r_*), \quad (44)$$

where $-F_{N,R}(\lambda, k, r)$ is the logarithm of the integrand in (43), and $r = r_*$ is a saddle point of $F_{N,R}(\lambda, k, r)$ given by

$$\left. \frac{\partial}{\partial r} F_{N,R}(\lambda, k, r) \right|_{r=r_*} = 0. \quad (45)$$

Here, by using the expression (5) in the leading order of $1/R$, $F_{N,R}^{1/R,leading}(\lambda, k, r)$ is given by

$$F_{N,R}^{1/R,leading}(\lambda, k, r) := -f_0 - (NR - 1) \log r + A_0 \log(1 + A_1 r^6) + B_0 \log(1 + B_1 r^6) + kr^2 \quad (46)$$

with

$$\begin{aligned} f_0 &= \log V_{NR-1}, \\ A_0 &= \frac{N(N-1)(N+4)}{12}, \quad A_1 = \frac{12\lambda}{N^3 R^2}, \\ B_0 &= \frac{N}{2}, \quad B_1 = \frac{6(N+4)\lambda}{N^3 R^2}. \end{aligned} \quad (47)$$

Let us first show that there exists a unique solution to the saddle point equation (45) for the leading order expression (46) in the integration region $r \geq 0$ of (43). To see this, it is convenient to use a new parametrization of R in terms of α as $R = R_c(1 + \alpha)$ with $R_c = (N+1)(N+2)/2$ and $-1 < \alpha$. Then, by noting $NR_c = 6(A_0 + B_0)$, the saddle point equation (45) with (46) can be written as

$$NR_c \alpha - 1 + \frac{6A_0}{1 + A_1 r_*^6} + \frac{6B_0}{1 + B_1 r_*^6} = 2kr_*^2. \quad (48)$$

The lefthand side is obviously a decreasing function of r_* with a maximum at $r_* = 0$, while the righthand side is an increasing function from zero to the infinity. Since the maximum on the lefthand side is $NR_c \alpha - 1 + 6A_0 + 6B_0 = NR - 1$, there always exists a unique solution of r_* for $N, R \geq 1$. Moreover, the solution is smooth: r_* does not jump in a discrete manner, when the parameters are continuously changed, because the r_* -dependence of each side continuously changes. This turns down the possibility that the model has a discontinuous phase transition in this treatment.

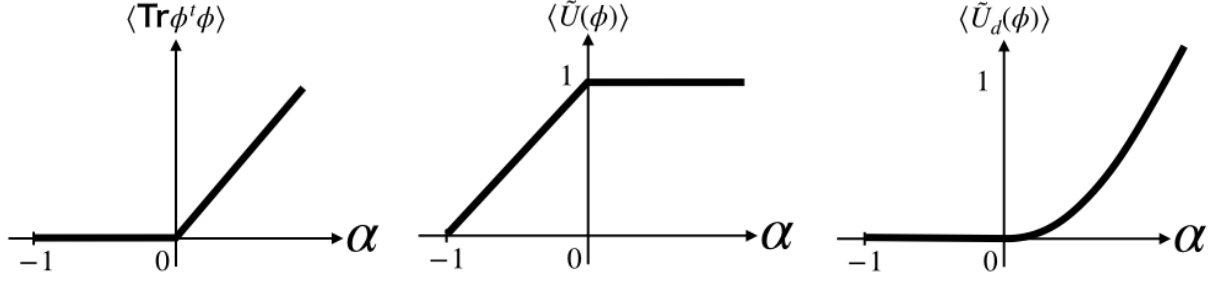


Figure 2: The behavior of the observables with respect to $\alpha = (R - R_c)/R_c$ in the large N limit, based on the saddle point analysis of the leading order in $1/R$. The parameters are assumed to be $\lambda \sim O(1)$ and $k \lesssim O(1)$.

To discuss the solution more quantitatively with approximations, let us restrict ourselves to the parameter range of our interest: $\lambda \sim O(1)$, $N \gtrsim O(10)$, and $k \lesssim O(1)$. In addition, for the simplicity of the following discussions, let us avoid the region around $\alpha \sim 0$. By noting that NR_c , and A_0 are of order $O(10^3)$ or larger, one can find that, for each case of $\alpha < 0$ and $\alpha > 0$, there are only two relevant terms among all in (48). For $\alpha < 0$, the first and third terms on the lefthand side are relevant, and for $\alpha > 0$, the first term on the lefthand side and the one on the righthand side are relevant. By solving the equations under these simplifications, the solutions are respectively given by

$$r_*^2 \sim \begin{cases} \left(\frac{1}{A_1} \left(-\frac{6A_0}{NR_c\alpha} - 1 \right) \right)^{\frac{1}{3}}, & \alpha < 0, \\ \frac{NR_c\alpha}{2k}, & \alpha > 0. \end{cases} \quad (49)$$

The first case shows divergent behavior for $\alpha \rightarrow -0$. However, this should not be taken as it is, since the transition should not have such an abrupt behavior as discussed above. In fact, the simplification taken above brakes down in the vicinity of $\alpha \sim 0$, and the real behavior is such that r_*^2 smoothly interpolates between the two parameter regions in the vicinity of $\alpha \sim 0$.

The r_*^2 in (49) has different large- N behavior in the two regions: $N^{\frac{7}{3}}$ for $\alpha < 0$ and N^3 for $\alpha > 0$. By normalizing r_*^2 with the common factor $(NR_c)^{-1}$ for both the regions, we obtain

$$\tilde{r}_*^2 \sim \begin{cases} 0, & \alpha \leq 0, \\ \frac{\alpha}{2k}, & \alpha > 0, \end{cases} \quad (50)$$

in the $N \rightarrow \infty$ limit, where $\tilde{r}_*^2 := (NR_c)^{-1}r_*^2$. See the leftmost figure in Figure 2. This characterizes the transition at $\alpha = 0$ as a continuous phase transition with $\langle \text{Tr}(\phi^t \phi) \rangle / (NR_c) = 0$ for $\alpha \leq 0$ and $\langle \text{Tr}(\phi^t \phi) \rangle / (NR_c) > 0$ for $\alpha > 0$.

The other observables can be treated in similar manners. By taking (9), putting $r = r_*$,

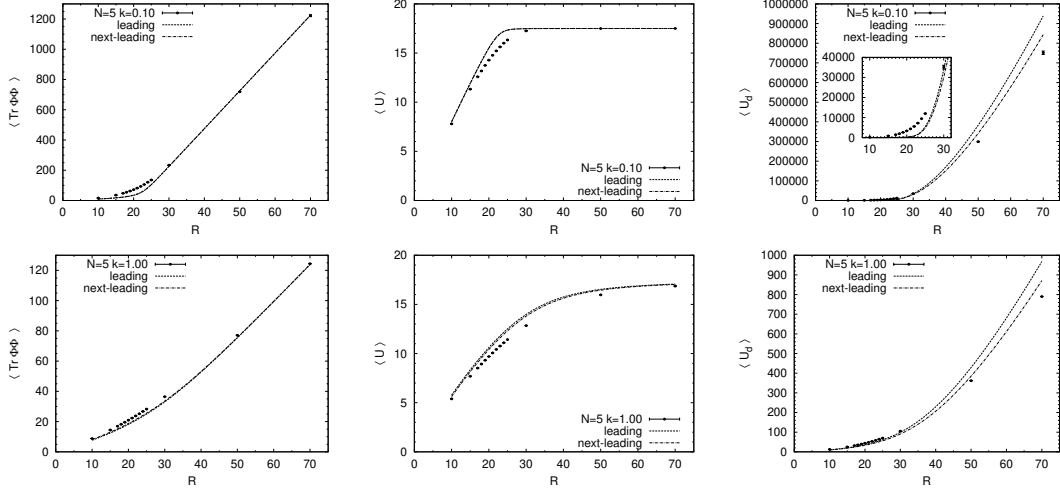


Figure 3: The numerical results of e.v. of the observables given in Eq.(12) for $N = 5$ and $k = 0.1$ (top three) and $k = 1.0$ (bottom three) against R . Plotted points represent the Monte Carlo results and ‘leading’ and ‘next-leading’ mean the evaluations based on Eq.(12) with perturbatively evaluated $f_{N,R,\lambda,\lambda_d}(t)$ in the leading and next-leading orders, respectively.

and taking the leading order in large N , one obtains

$$\begin{aligned} \langle U(\phi) \rangle_{\text{leading}} &\sim \begin{cases} \frac{N^3}{12\lambda}(1+\alpha), & \text{for } \alpha \leq 0, \\ \frac{N^3}{12\lambda}, & \text{for } \alpha > 0, \end{cases} \\ \langle U_d(\phi) \rangle_{\text{leading}} &\sim \begin{cases} \frac{N^3(1+\alpha)}{12\lambda(-\alpha)}, & \text{for } \alpha \leq 0, \\ \frac{N^5}{16k^3} \frac{\alpha^3}{(1+\alpha)^2}, & \text{for } \alpha > 0. \end{cases} \end{aligned} \quad (51)$$

The divergence of $\langle U_d(\phi) \rangle_{\text{leading}}$ in $\alpha \rightarrow -0$ should not be taken as it is, because of the same reason mentioned above for r_*^2 . By normalizing $\tilde{U}(\phi) := (N^3/12\lambda)^{-1}U(\phi)$ and $\tilde{U}_d(\phi) := (N^5/16k^3)^{-1}U_d(\phi)$, one obtains

$$\begin{aligned} \langle \tilde{U}(\phi) \rangle_{\text{leading}} &\sim \begin{cases} 1+\alpha, & \text{for } \alpha \leq 0, \\ 1, & \text{for } \alpha > 0, \end{cases} \\ \langle \tilde{U}_d(\phi) \rangle_{\text{leading}} &\sim \begin{cases} 0, & \text{for } \alpha \leq 0, \\ \frac{\alpha^3}{(1+\alpha)^2}, & \text{for } \alpha > 0. \end{cases} \end{aligned} \quad (52)$$

See the middle and rightmost figures in Figure 2. The result supports the same conclusion that there is a continuous phase transition at $\alpha = 0$.

6 Comparison with Monte Carlo simulations

In Section 4, we have computed the leading order approximation of $f_{N,R,\lambda,\lambda_d}(t)$ defined in (11) in a perturbative method, and have obtained the result (14) along with (15) and so on. We

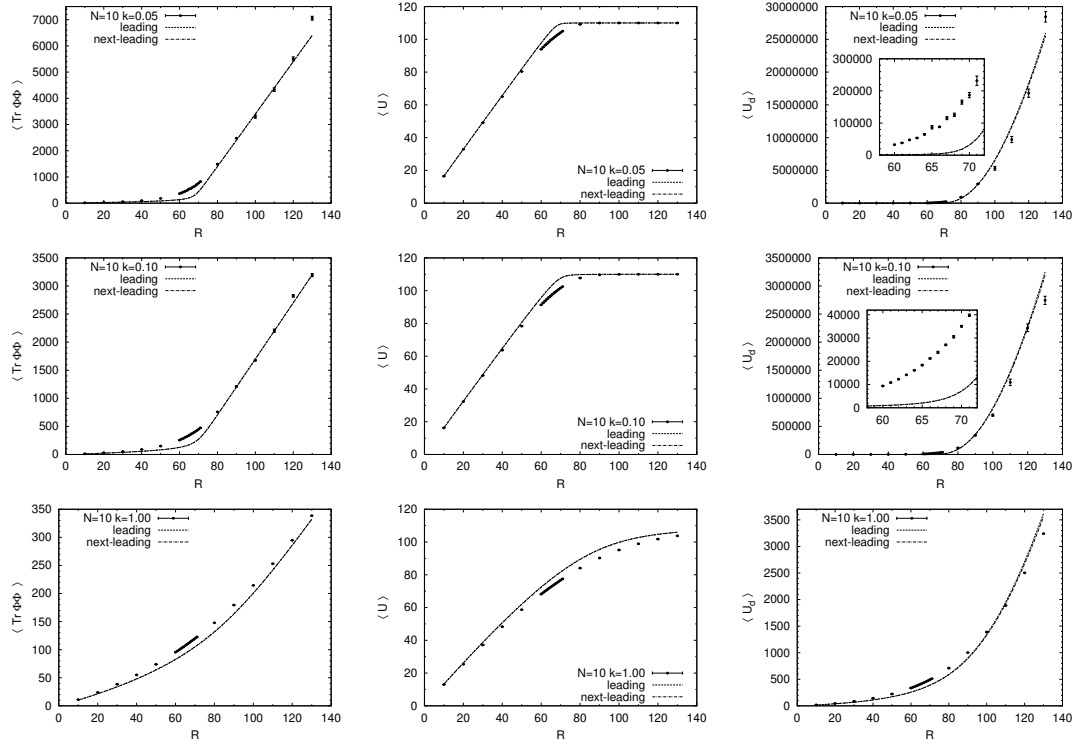


Figure 4: $N = 10$ and $k = 0.05$ (top three), $k = 0.10$ (middle three) and $k = 1.00$ (bottom three) against R . The same notations are used as in Figure 3.

have also derived the next-leading order correction (41) with (42), the details of which are given in Appendix C. With those results, we can numerically calculate the expectation values (e.v.) of the observables given in (12) by the expressions on the righthand sides. However, note that the above approximations of $f_{N,R,\lambda,\lambda_d}(t)$ are based on taking the perturbative expansion of S_{eff} given in (27) up to the second order in t . Therefore they require the implicit assumption of small values of t , and may not generally be trusted for the computation of (12), because t is finally assigned with r^6 , and r is integrated over zero to infinity.

In view of the question above, it would be interesting to compute our model without any adoption of approximation methods. More specifically, in this section we compute the e.v. of the observables, (6) with $\mathcal{O}(\phi) = \text{Tr}(\phi^t \phi), U(\phi), U_d(\phi)$, by the Monte Carlo simulations, and compare them with the results obtained by numerically integrating the righthand sides of (12), where we put our perturbative results for $f_{N,R,\lambda,\lambda_d}(t)$. Note that, in our strategy of the approximations, R is not an expansion parameter, only t is, and therefore it is meaningful to compare the results in the full range of R .

The results of the comparison are summarized in Figures 3 and 4. The points, each with an error bar (though it's very small), represent the Monte Carlo results. For the information about the parameters taken in the Monte Carlo simulations, refer to the captions. The dotted and chained lines represent the values of the e.v. of the observables in the leading and the next-leading orders by adopting $f_{N,R,\lambda,\lambda_d}(t)^{\text{leading/next-leading}}$ to (12), respectively. In some figures, it is difficult to distinguish these two lines, almost overlapping with each other.

An important thing that can be observed in the figures is that, for each N , there exists a region of R where the behavior of the observables changes between that for smaller R and for larger R . This is more clearly seen for larger N and smaller k . The transition region we observe indeed exists around the value $R_c = (N+1)(N+2)/2$, which was obtained from the saddle point analysis in Section 5 (See Figure 2.). It is an important physical question whether this transition of behavior is a phase-transition or just a crossover in the thermodynamic limit.

However, we cannot currently answer this question for certain with the Monte Carlo results presently available, and this would require larger scale Monte Carlo simulations. It seems also difficult to answer this question by our perturbative analytical methods because of the following reason. In the figures, we can find good agreement between the perturbative computations and the Monte Carlo results in the regions away from the transition region. This would support the validity of our perturbative calculations in those outside regions. On the other hand, we can observe that there exist some deviations between the perturbative computations and the Monte Carlo results in the transition region. The deviations are such that the Monte Carlo results smoothen the transition to make it more like a crossover. Therefore, the analytical expressions we have obtained as approximations do not seem to be reliable in the transition region.

We can further discuss this complication from another view point as follows. Let us look more closely into the numerical data, though we do not explicitly show those values here. We can find that, as to the numerical relations among $\langle \text{Tr} \phi^t \phi \rangle$, $\langle U \rangle$, and $\langle U_d \rangle$ in the leading and

the next-leading orders, the following hold:

$$\begin{aligned}
\langle \text{Tr } \phi^t \phi \rangle &: \text{including next-leading} > \text{leading}, \\
\langle U \rangle &: \text{including next-leading} < \text{leading}, \\
\langle U_d \rangle &: \text{including next-leading} < \text{leading},
\end{aligned} \tag{53}$$

for all R . Therefore, while the next-leading order corrections indeed improve the approximations so that they approach the Monte Carlo results in the outside regions and this is also so for $\langle \text{Tr } \phi^t \phi \rangle$ and $\langle U \rangle$ in the transition region, the last inequality about $\langle U_d \rangle$ is in the opposite direction. This suggests that our perturbative treatment seems to have some difficulties in correctly taking into account some configurations that mainly contribute to U_d in the transition region. It would be an interesting future problem to identify these configurations.

Lastly, let us briefly explain our actual Monte Carlo simulations. We have performed Monte Carlo simulations with the standard Metropolis update method for the model (1) by using KEKCC, the cluster system of KEK. For each calculation shown in the figures, we performed 2 billion sweeps, where the time taken for this was generally about 7 and 23 hours with $R = 10$ and 130, respectively. We stored the data of the observables once per 400 sweeps, and computed their mean values and the 1σ -errors by the Jackknife resampling method. In each calculation we always set the acceptance rate to be around 60%. However, to realize this 60%, we had to tune the step sizes in our Metropolis method to quite small values, especially in the region $R \gtrsim N^2/2$.

Let us further comment on the last peculiar nature we encountered in the simulations. We have performed the simulations for $k = 1, 0.1, 0.05$ with $N = 10$ and $k = 1.0, 0.1$ with $N = 5$, respectively, as shown in the figures. As suggested by the results in the figures, the transition could be sharpened, if we performed simulations with smaller values of k than those in the figures. However, when we tried to do so, we encountered a serious difficulty in particular in the region $R \gtrsim N^2/2$. It was that the Metropolis step sizes must be tuned to very small values to keep the reasonable acceptance rate like 60%. Then, the performance of the simulations became so slow that we could not find the timing when the system had reached thermodynamic equilibriums: The system always looked like being in the middle stage of moving very slowly toward thermodynamic equilibriums, at least during one week of continuous running or so. Therefore we took relatively large values of k as those in the figures to avoid the serious difficulty that makes the simulations unreliable.

7 Topological structure of configurations

In this section, we will explain our observation on the topological structure of the configurations generated by the Monte Carlo simulations. Topology of a value of the matrix ϕ_a^i can be analyzed by persistent homology, which is a modern technique of the topological data analysis (See Appendix D for a brief introduction of persistent homology.). More specifically, we performed the Monte Carlo simulations for $N = 4$ and $R = 10, 15, 20, 25$ with $\lambda = 1$, $k = 0.01$, and, for each case, uniformly took 100 samples of the values of ϕ_a^i during a large number of

sequential updates of order 10^8 after thermodynamic equilibriums were seen to be reached. Then, the samples are analyzed in terms of persistent homology. The analysis shows that the favored topology of the configurations is S^1 for $R = 10, 15$, but gradually changes to higher dimensional cycles, when R is increased. We will first explain the background motivation for this analysis, and will then show the results.

One of the present authors and his collaborators have been studying a tensor model in the canonical formalism, which we call canonical tensor model [16, 17], as a model of quantum gravity. In [18], it has been shown that the exact wave function of the tensor model has peaks at the configurations that are invariant under Lie groups. This phenomenon, which we call symmetry highlighting phenomenon, potentially has an important physical significance, since this phenomenon would imply the dominance of spacetimes symmetric under Lie groups through the correspondence between tensors and spaces developed in [19]. This symmetry highlighting phenomenon has first been shown for a toy wave function [20], which slightly simplifies the wave function of the canonical tensor model. The toy wave function is given by⁷

$$\Psi(P) = \int_{\mathbb{R}^N} \prod_{a=1}^N d\phi_a \exp (IP_{abc}\phi_a\phi_b\phi_c + (I\kappa - \epsilon)\phi_a\phi_a), \quad (54)$$

where I denotes the imaginary unit, and ϵ is a small positive regularization parameter to assure the convergence of the integral (This regularization method is often called Feynman prescription). The symmetry highlighting phenomenon is that the wave function has large peaks at P_{abc} that are invariant under Lie groups: $P_{abc} = h_a^{a'}h_b^{b'}h_c^{c'}P_{a'b'c'}$ under $\forall h \in H$, where H is a representation of a Lie group. The phenomenon can qualitatively be understood by the following rough argument: If P_{abc} is invariant under a Lie group, the integration over ϕ_a in (54) will contribute coherently along the gauge orbit $h_a^{a'}\phi_{a'}$ ($\forall h \in H$), while otherwise the contributions tend to cancel among themselves due to the phase oscillations of the integrand and the wave function takes relatively small values. In [20], some tractable simple cases have explicitly been studied, indeed showing the presence of the phenomenon.

Other than the simple case studies, the peak structure of the toy wave function and that of the tensor model are largely unknown. One reason is that the number of independent components of P_{abc} , which is about $\sim N^3/6$, is so large that it is practically not possible to go over the whole configuration space of P_{abc} . Rather, we will be able to obtain the rough knowledge by integrating over P_{abc} :

$$\int_{-\infty}^{\infty} \prod_{a \leq b \leq c=1}^N dP_{abc} \Psi(P)^R \exp(-\alpha P_{abc}P_{abc}) = \text{const.} Z_{N,R} \left(\frac{1}{4\alpha}, -I\kappa + \epsilon \right), \quad (55)$$

where we consider an arbitrary power R of the wave function, because the actual wave function

⁷This wave function has actually the same form as the spherical p -spin model [27, 28] except for the following differences: The coupling constants of the former are pure imaginary, while they are real for the latter; There is a spherical constraint $\phi_a\phi_a = \text{const.}$ in the latter, while there is none in the former. In addition, $R \rightarrow 0$ is taken in the study of the latter for the replica trick, but we have to take $R \sim N^2/2$ for the consistency of the tensor model.

of the tensor model has a corresponding power,⁸ which is given by $R = (N + 2)(N + 3)/2$ [18, 15, 29]. In (55), we see that the integration over P_{abc} with a Gaussian weight produces our model (1). Since the integration sums over all the contributions of the peaks (and the backgrounds as well), we expect that, in the present model, the replicated configurations ϕ_a^i ($i = 1, 2, \dots, R$) will tend to exist along some gauge orbits.

In general, there exists a number of peaks (or rather ridges) associated with various symmetries and gauge orbits for a given wave function (54). As argued and shown explicitly in [20, 18], peaks associated with lower dimensional Lie group symmetries generally exist more widely than those with higher dimensional symmetries, because the number of symmetry conditions that must be satisfied by P_{abc} is smaller for the former than for the latter. On the contrary, peaks of the latter are generally higher than those of the former, because the dimensions of gauge orbits of the latter are larger providing more coherent contributions than the former. Therefore, there are competitions between height and proliferation, and it is generally a subtle question which of lower or higher dimensional Lie group symmetries is probabilistically favored in a given case.

For (55) of our interest, the answer to this question concerning dominance will depend on the value of the parameter R . As R is the power of the wave function as in (55), larger R will enhance higher peaks compared to the lower ones. Therefore what can be expected is that, for larger R , peaks with higher dimensional symmetries will dominate because of the enhancement of the peaks, but for smaller R , peaks with lower dimensional Lie group symmetries will dominate because of their wide existence. In addition, when R is small enough, even non-symmetric configurations will dominate, since they exist most widely.

In the Monte Carlo simulation of our model, if a symmetric peak dominates as explained above, configurations ϕ_a^i will be distributed along the associated gauge orbit. A gauge orbit exists in the vector space associated to the lower index of ϕ_a^i . Since the upper index represents the replicas, the expected outcome is that the R vectors, ϕ_a^i ($i = 1, 2, \dots, R$), are randomly distributed on the gauge orbit. A caution here is that the gauge orbit associated to a tensor with a symmetry H can change its location by $O(N)/H$ in the vector space, depending on the actual value of the tensor. Therefore, to see the presence of such a gauge orbit, we have to see it for each sample of ϕ_a^i ($i = 1, 2, \dots, R$), not by plotting all the samples in one vector space. This will require larger R to detect higher dimensional gauge orbits. Another caution is that what we can find is a mixture of these contributions from a number of peaks, making the outcome to be statistical distributions.

Topological structure of each sample of ϕ_a^i can be analyzed by using persistent homology. This is a modern applied mathematical technique of the topological data analysis, and can extract homology groups of a data (See Appendix D.). Here an input data is supposed to be described by a set of points that have relative distances. We used an open-source c++ program that is called Ripser⁹ for the analysis and plotted the output with Mathematica. For

⁸The corresponding power may rather be $R = R_c = (N + 1)(N + 2)/2$ than what is in the text, because one of the integration variables is fixed in the toy wave function compared to the actual wave function of the tensor model. This slight difference is not important at the present stage of study, but may become so in the future.

⁹This open-source software can be downloaded from <https://github.com/Ripser/riper>.

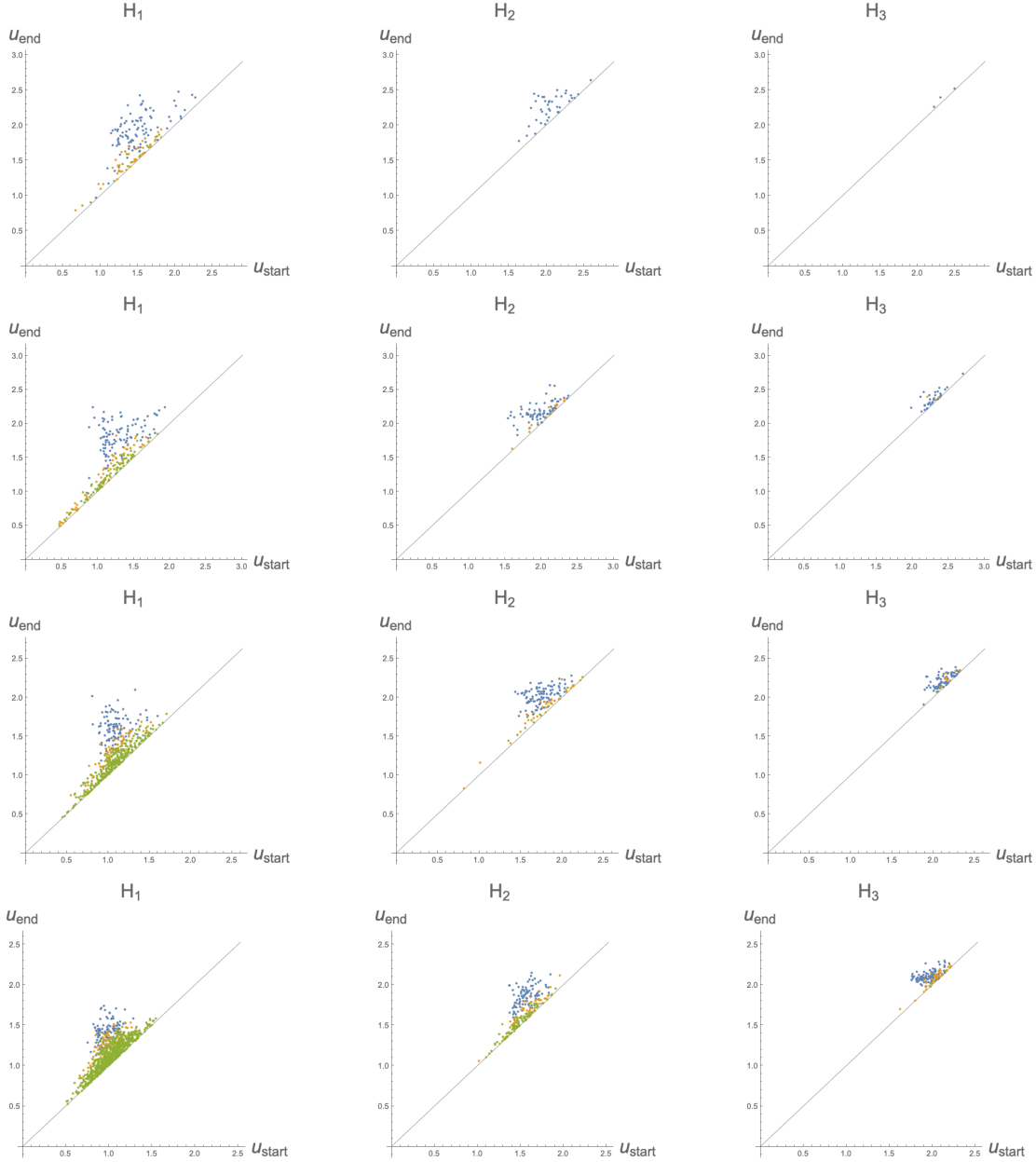


Figure 5: Persistent diagrams obtained from the Monte Carlo data of $N = 4$, $k = 0.01$, $\lambda = 1$ with $R = 10, 15, 20, 25$ (from the top to the bottom). To avoid the dependence of the initial values, 10 independent Monte Carlo sequences were run, and the sampling were performed uniformly from the sequence of updates of $\sim 10^9$ after thermodynamic equilibriums were seen. 100 configurations of ϕ_a^i were uniformly sampled and the persistent homologies were analyzed (one- to three-dimensional homologies from the left to the right). The results of 100 samples are plotted on the same persistent diagrams. Blue dots represent the longest-life elements in each dimensional persistent homology group of each data, the yellow ones the second, and the green ones all after the second. The dots away from the diagonal line represent long-life persistent homology group elements, which are considered to be characteristics of a data, while those near the diagonal line are regarded as “noises”. The highest blue dots, namely those with the largest u_{end} that represent the largest structure, move from H_1 to H_3 with the increase of R .

a configuration ϕ_a^i , we consider the replica number $i = 1, 2, \dots, R$ to represent the label of “points” of a data set, and define the distances between two points i and j as

$$d(i, j) := \arccos \left(\frac{\phi_a^i \phi_a^j}{\sqrt{\phi_a^i \phi_a^i \phi_b^j \phi_b^j}} \right). \quad (56)$$

The gist of this definition is that the N -dimensional vectors ϕ_a^i ($i = 1, 2, \dots, R$) are projected onto the unit sphere S^{N-1} , and the geodesic distances among them are measured.

We want to see the phenomenon explained above from the actual data of the Monte Carlo simulation. For this initial study, choosing small N would be preferred for simpler analysis, because then there exist a small number of possibilities of gauge orbits, and also thermodynamic equilibriums can easily be reached due to the small number of degrees of freedom. Note however that, as explained above, this trades off the clarity of the homology structure since the range of R where the phenomenon appears will become smaller for smaller N , and the number R of points may not be enough to well cover higher dimensional gauge orbits.

For the actual simulation, we considered $N = 4$. In $N = 4$, as explicitly solved in [20], there exist only two possibilities of Lie group symmetries, $SO(2)$ and $SO(3)$, and the gauge orbits are S^1 and S^2 , respectively. In fact, the ridges of the P_{abc} with these symmetries reach the origin $P_{abc} = 0$, and therefore we can also add the trivial possibility of S^3 with the $SO(4)$ symmetry, which is the maximal possibility for $N = 4$. Figure 5 shows the persistent diagrams obtained from the Monte Carlo simulations with $R = 10, 15, 20, 25$. Statistically speaking, one can observe that, starting from S^1 at $R = 10, 15$, higher dimensional cycles gradually appear and become the largest structure when R is increased (while lower dimensional cycles take smaller values of u).

8 Summary and future prospects

In this paper, we studied a matrix model containing non-pairwise index contractions [21], which has a motivation from a tensor model of quantum gravity [16, 17]. This matrix model has the same form as what appears in the replica trick of the spherical p -spin model for spin glasses [27, 28], though the parameter range of our interest is different. More specifically, it has ϕ_a^i ($a = 1, 2, \dots, N$, $i = 1, 2, \dots, R$) as its degrees of freedom, where the lower indices are pairwise contracted, but the latter are not always done so. We performed Monte Carlo simulations with the Metropolis update method, and compared the results with some analytical computations in the leading order, mostly based on the previous treatment in [21]. They are in good agreement outside the transition region located around $R \sim N^2/2$. In the transition region, however, there exist deviations between the simulations and the analytical results, and the deviations cannot be corrected well, even if the next-leading order contributions are included. It has not been determined whether the transition is a phase transition or a crossover, because of the limited range of the parameters like $N \lesssim 10$ available in our Monte Carlo

simulation. Our Monte Carlo simulation tended to stack especially at $R \gtrsim N^2/2$, suspecting that the system gets glassy nature in the region, but no conclusive argument has been made for this aspect. We also studied the topological characteristics of the configurations generated in the Monte Carlo simulations by using the modern technique called persistent homology [30] in topological data analysis. This technique extracts the homology structure of a data, which is a configuration of ϕ_a^i in our case. We observed that, in the vicinity of the transition region, the homology structure of the configurations gradually changes from S^1 to higher-dimensional cycles with the increase of R .

A particularly interesting result of this paper is that there seems to exist a transition region around $R \sim N^2/2$. Intriguingly, this value of R coincides with what is required by the consistency of the tensor model (namely, the hermiticity of the hamiltonian constraint) [18, 15, 29]. Moreover, some questions about this region are left unanswered: There are some deviations between the simulation and the analytical results in this region, but the reason is not clear; The transition of the homological structure of the dominant configurations in this vicinity is peculiar but not well understood; Whether the transition is a phase transition or a crossover is not determined. Thus, our model seems to be most interesting around this region, but most of the properties are not well understood. For the better understanding in the future, it seems necessary to treat larger N cases by employing more efficient methods of Monte Carlo simulations and finding more powerful analytical methods.

Acknowledgements

The Monte Carlo simulations in this study were performed using KEKCC, the cluster system of KEK. The work of N.S. is supported in part by JSPS KAKENHI Grant No.19K03825.

Appendices

A $R = 2$ case

In this appendix, we consider the partition function for $R = 2$, and see that the partition function is finite even for $k = 0$. This is not trivial, because, for general $R > 1$, the solution to $U(\phi) = 0$ is non-empty (see below), and therefore there is a potential risk of runaway behavior, $\phi^2 \rightarrow \infty$ with $U(\phi) = 0$.

Let us first see that $U(\phi) = 0$ is non-empty for general $R > 1$. Since

$$U(\phi) = \left(\sum_{i=1}^R \phi_a^i \phi_b^i \phi_c^i \right) \left(\sum_{j=1}^R \phi_a^j \phi_b^j \phi_c^j \right), \quad (57)$$

$U(\phi) \geq 0$ holds, and $U(\phi)$ vanishes iff

$$\sum_{i=1}^R \phi_a^i \phi_b^i \phi_c^i = 0. \quad (58)$$

An obvious set of solutions are given by $\phi_a^{2i-1} = -\phi_a^{2i}$, ($i = 1, 2, \lfloor R/2 \rfloor$) with $\phi_a^R = 0$ if R =odd.

For $R = 2$, one can see that this is the only solution as follows. By contracting the indices b and c in (58), we obtain

$$\phi_a^1 \phi_b^1 \phi_b^1 + \phi_a^2 \phi_b^2 \phi_b^2 = 0. \quad (59)$$

This implies that ϕ^1 and ϕ^2 are linearly dependent, and putting this back to (58), we obtain $\phi_a^1 = -\phi_a^2$.

In the $R = 2$ case, since $U(\phi)$ depends only on the relative directions and the sizes of ϕ_a^1 and ϕ_a^2 , the partition function for $k = 0$ can be written as

$$Z_{N,R=2}(\lambda, k=0) = \text{Vol}(S^{N-1}) \text{Vol}(S^{N-2}) \int_0^\infty dr_1 dr_2 r_1^{N-1} r_2^{N-1} \int_0^\pi d\theta \sin^{N-2}(\theta) e^{-\lambda U(\theta)}, \quad (60)$$

where

$$U(r_1, r_2, \theta) = r_1^6 + r_2^6 + 2r_1^3 r_2^3 \cos^3(\theta) \quad (61)$$

with r_1 and r_2 being the sizes, and θ being the relative angle. As shown above, the only case with $U = 0$ is given by $r_1 = r_2$, $\theta = \pi$. Therefore let us perform the reparameterization,

$$r_1 = r, \quad r_2 = r(1+x), \quad \theta = \pi - y. \quad (62)$$

Then the integral of (60) at large r can be approximated by expanding the integrand for small x, y , and we obtain

$$\sim \int dr dx dy r^{2N-1} y^{N-2} e^{-3\lambda r^6(3x^2+y^2)} \sim \int dr r^{-N-1}. \quad (63)$$

This shows that the partition function is convergent for $R = 2$ and $k = 0$.

There are two things which can be learned from this simplest case. One is that, if R is small enough, the partition function is convergent even for $k = 0$. Another thing is that the large- r asymptotic behavior of the integrand is much slower than the leading order result,

$$\int dr r^{NR-1} f_{N,R}^{\text{leading}}(\lambda r^6) \sim \int dr r^{2N-1-N(N+1)(N+2)/2}. \quad (64)$$

Therefore the asymptotic behavior derived from the leading order result cannot be correct down to $R = 2$.

B Derivation of (29)

In this section, we derive (29). This was previously derived in [21], but this is repeated here to make the present paper self-contained.

For $m = \text{odd}$, the equation holds, because the both sides vanish.

Let us assume $m = 2p$ with a positive p . Let us start with the following equation:

$$\frac{1}{\int_{S^{NR-1}} d\tilde{\phi}} \int_{S^{NR-1}} d\tilde{\phi} \tilde{\phi}_{a_1}^{i_1} \tilde{\phi}_{a_2}^{i_2} \cdots \tilde{\phi}_{a_{2p}}^{i_{2p}} = \frac{1}{\int_{\mathbb{R}^{NR}} d\phi e^{-\beta \text{Tr} \phi^t \phi}} \int_{\mathbb{R}^{NR}} d\phi \frac{\phi_{a_1}^{i_1} \phi_{a_2}^{i_2} \cdots \phi_{a_{2p}}^{i_{2p}}}{(\text{Tr} \phi^t \phi)^p} e^{-\beta \text{Tr} \phi^t \phi}, \quad (65)$$

where β is an arbitrary positive constant. This can easily be proven by reparameterizing ϕ_a^i with the radial and the angular variables as $\phi_a^i = r \tilde{\phi}_a^i$ on the righthand side, and observing that the integrations over r decouples from the angular part and cancels between the numerator and the denominator.

Let us consider the numerator on the righthand side of (65),

$$A(\beta) := \int_{\mathbb{R}^{NR}} d\phi \frac{\phi_{a_1}^{i_1} \phi_{a_2}^{i_2} \cdots \phi_{a_{2p}}^{i_{2p}}}{(\text{Tr} \phi^t \phi)^p} e^{-\beta \text{Tr} \phi^t \phi}. \quad (66)$$

Taking the p -th derivative of $A(\beta)$ with respect to β cancels the $(\text{Tr} \phi^t \phi)^p$ in the denominator of the integrand. On the other hand, by performing the rescaling $\phi_a^i \rightarrow \beta^{-1/2} \phi_a^i$, it is obvious that $A(\beta)$ has the dependence $\beta^{-NR/2}$ on β . Therefore, by performing the p -th derivative of the both sides of (66), we obtain the relation,

$$\frac{\Gamma\left(\frac{NR}{2} + p\right)}{\Gamma\left(\frac{NR}{2}\right)} \beta^{-p} A(\beta) = \int_{\mathbb{R}^{NR}} d\phi \phi_{a_1}^{i_1} \phi_{a_2}^{i_2} \cdots \phi_{a_{2p}}^{i_{2p}} e^{-\beta \text{Tr} \phi^t \phi}. \quad (67)$$

By solving for $A(\beta)$ and putting it into (65), we obtain (29).

C Computation of $f_{N,R,\Lambda_{ij}}(t)$ in the next-leading order

In this appendix, we will compute the fourth-order term $\langle (P\tilde{\phi}^3)^4 \rangle_\phi^c$ in (27). From the definition (25) of cumulants and the formula (29), we obtain

$$\begin{aligned} \langle (P\tilde{\phi}^3)^4 \rangle_\phi^c &= \langle (P\tilde{\phi}^3)^4 \rangle_{\tilde{\phi}} - 3(\langle (P\tilde{\phi}^3)^2 \rangle_{\tilde{\phi}})^2 \\ &= \gamma_6 (2\beta)^6 \langle (P\phi^3)^4 \rangle_\phi - 3(\gamma_3 (2\beta)^3 \langle (P\phi^3)^2 \rangle_\phi)^2 \\ &= \gamma_6 (2\beta)^6 \langle (P\phi^3)^4 \rangle_\phi^c - 3(2\beta)^6 (\gamma_3^2 - \gamma_6) (\langle (P\phi^3)^2 \rangle_\phi^c)^2. \end{aligned} \quad (68)$$

The $\langle (P\phi^3)^2 \rangle_\phi^c$ in the last term has already been computed in Section 4. As for $\langle (P\phi^3)^4 \rangle_\phi^c$, Wick contractions (31) give the five connected diagrams in Figure 6. By counting the number of ways to connect the legs, one can find that the degeneracies are given by $2^3 \cdot 3^5$, $2^4 \cdot 3^5$,

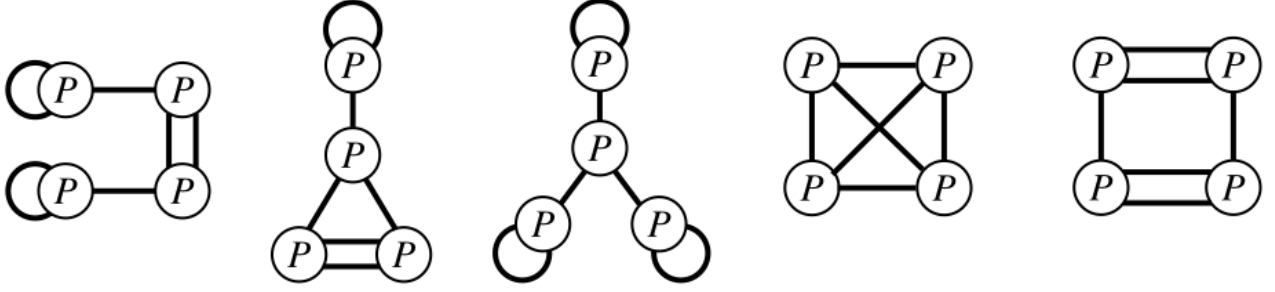


Figure 6: The Feynman diagrams for the forth order interaction term, $\langle (P\phi^3)^4 \rangle_\phi^c$, in the effective action $S_{eff}(P)$ in (27).

$2^3 \cdot 3^4$, $2^4 \cdot 3^4$, and $2^3 \cdot 3^5$, respectively, from the left to the right diagrams¹⁰ in Figure 6. These Feynman diagrams represent the way of the index contractions of P_{abc}^i 's in the fourth order interaction term. For example, the leftmost diagram gives

$$\langle (P\phi^3)^4 \rangle_\phi^{c, \text{leftmost}} = \frac{2^3 3^5}{(2\beta)^6} \sum_{i_1, i_2, i_3, i_4, j=1}^R \tilde{\Lambda}_{i_1 j} \tilde{\Lambda}_{i_2 j} \tilde{\Lambda}_{i_3 j} \tilde{\Lambda}_{i_4 j} P_{aab}^{i_1} P_{bcd}^{i_2} P_{cde}^{i_3} P_{eff}^{i_4}, \quad (69)$$

where the numerator of the numerical factor is the degeneracy, and the denominator comes from the factor of the Wick contraction (31). It is also straightforward to write down the explicit expressions for all the other diagrams in Figure 6.

Now let us suppose we have obtained the explicit expressions of $S_{eff}^{(4)}(P)$ by the above procedure. An immediate difficulty of this forth order term is that $S_{eff}^{(4)}(P)$ has the negative all over sign due to I^4 as in (27), and therefore the system with $S_{eff}(P) = S_{eff}^{(2)}(P) + S_{eff}^{(4)}(P)$ is not stable. This may be changed if we incorporate the next order term $S_{eff}^{(6)}(P)$, which has a positive coefficient, but the computation will become more complicated than $S_{eff}^{(4)}(P)$ and will not be performed in this paper. To treat this situation in a consistent manner, we only take the first correction coming from $S_{eff}^{(4)}(P)$ as $e^{-S_{eff}^{(4)}(P)} \sim 1 - S_{eff}^{(4)}(P)$ rather than the full exponential form. Note that this can consistently be understood as taking the first correction coming from the full expression of the interactions, $e^{-S_{eff}^{(4)}(P) - S_{eff}^{(6)}(P) - \dots} = 1 - S_{eff}^{(4)}(P) - S_{eff}^{(6)}(P) + 1/2 S_{eff}^{(4)}(P)^2 - \dots$, in the order of t . Then $f_{N,R,\Lambda_{ij}}(t)$ with this first correction of the quartic order can be obtained by computing

$$\begin{aligned} f_{N,R,\Lambda_{ij}}^{(4)}(t) &= \text{const.} \int dP e^{-S_{eff}^{(2)}(P)} (1 - S_{eff}^{(4)}(P)) \\ &= f_{N,R,\Lambda_{ij}}^{(2)}(t) \left(1 - \langle S_{eff}^{(4)}(P) \rangle_P \right), \end{aligned} \quad (70)$$

¹⁰A non-trivial check of these numbers is to see whether the sum of them agrees with $12!/(2^6 \cdot 6!) - 3 \cdot 15^2$, where the former number counts all the possibilities of connecting 12 legs of the four vertices, and the latter is the subtraction of the disconnected diagrams among them.

$$A = \frac{1}{6} \left(\text{---} + \text{X} + \text{X} + \text{X} + \text{X} + \text{---} \right)$$

$$\tilde{B} = \text{> <}$$

Figure 7: Graphical representations of the matrices, A and \tilde{B} .

where $f_{N,R,\Lambda_{ij}}^{(2)}(t)$ is given in (39), the allover factor has been determined by requiring $f_{N,R,\Lambda_{ij}}^{(4)}(0) = 1$, and $\langle \cdot \rangle_P$ is defined by

$$\langle \mathcal{O}(P) \rangle_P := \frac{1}{\int dP e^{-S_{eff}^{(2)}(P)}} \int dP \mathcal{O}(P) e^{-S_{eff}^{(2)}(P)} \quad (71)$$

with the quadratic action $S_{eff}^{(2)}(P)$ given in (33).

The computation of $f_{N,R,\Lambda_{ij}}^{(4)}(t)$ in (70) has now been reduced to that of $\langle S_{eff}^{(4)}(P) \rangle_P$. This can be computed by the Wick theorem, using the Wick contraction for P_{abc}^i determined from $S_{eff}^{(2)}(P)$. This is obtained by taking the inverse of the coefficient matrix of the quadratic form $S_{eff}^{(2)}(P)$ of P_{abc}^i . Since $S_{eff}^{(2)}(P)$ has the form of the direct product with respect to the upper and lower indices, they can be treated separately.

Let us first treat the lower indices by starting with (36). Let us introduce the following matrices (See Figure 7):

$$A_{abc,def} = \frac{1}{6} \sum_{\sigma} \delta_{a\sigma_d} \delta_{b\sigma_e} \delta_{c\sigma_f}, \quad (72)$$

$$B_{abc,def} = \frac{3}{N+2} \left(A \tilde{B} A \right)_{abc,def}, \quad (73)$$

$$\tilde{B}_{abc,def} = \delta_{ad} \delta_{bc} \delta_{ef}, \quad (74)$$

where the summation over σ denotes the sum over all the permutations of d, e, f , and the product of two matrices, say X and Y , is defined by $(XY)_{abc,def} = \sum_{g,h,i=1}^N X_{abc,ghi} Y_{ghi,def}$. Note that A acts as an identity on a symmetric tensor, namely, $(AP)_{abc} = P_{abc}$. One can easily check the following properties:

$$A^2 = A, \quad AB = BA = B, \quad B^2 = B. \quad (75)$$

Furthermore, one can check that $A - B$ and B give the projectors to the tensor and vector parts of P_{abc} , respectively, as

$$(A - B)P = P^T, \quad BP = P^V. \quad (76)$$

Therefore, by using these matrices, (38) can be rewritten in the form,

$$P(c_{T,\lambda_{ev}}(A - B) + c_{V,\lambda_{ev}}B)P, \quad (77)$$

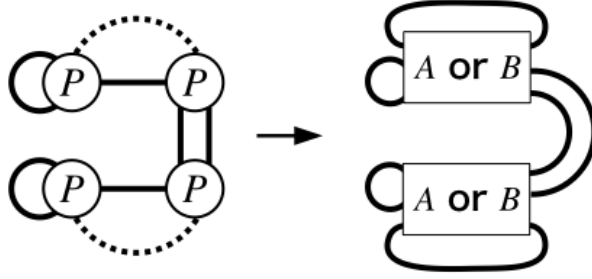


Figure 8: An example of Wick contraction of P_{abc}^i 's. This can be computed by inserting the matrices A and B at the location of the contraction.

where $c_{T,\lambda_{ev}}$ and $c_{V,\lambda_{ev}}$ are the coefficients associated to the tensor and vector parts of P_{abc} , namely,

$$\begin{aligned} c_{T,\lambda_{ev}} &= 1 + 12\gamma_3\lambda_{ev}t, \\ c_{V,\lambda_{ev}} &= 1 + 6(N+4)\gamma_3\lambda_{ev}t. \end{aligned} \quad (78)$$

The inverse of the matrix in (77) is given by

$$\begin{aligned} (c_{T,\lambda_{ev}}(A-B) + c_{V,\lambda_{ev}}B)^{-1} &= \frac{1}{c_{T,\lambda_{ev}}}(A-B) + \frac{1}{c_{V,\lambda_{ev}}}B \\ &= \frac{1}{c_{T,\lambda_{ev}}}A + \left(\frac{1}{c_{V,\lambda_{ev}}} - \frac{1}{c_{T,\lambda_{ev}}} \right) B. \end{aligned} \quad (79)$$

For later convenience, let us define

$$\begin{aligned} a_{\lambda_{ev}} &:= \frac{1}{c_{T,\lambda_{ev}}}, \\ b_{\lambda_{ev}} &:= \frac{1}{c_{V,\lambda_{ev}}} - \frac{1}{c_{T,\lambda_{ev}}}. \end{aligned} \quad (80)$$

Let us next take into account the upper indices. To derive the above result we started with the expression (36) with an eigenvalue λ_{ev} of the matrix Λ_{ij} . Therefore it is the result for the corresponding eigenspace. Considering the projection to each eigenspace, the final form of the Wick contraction for P_{abc}^i is obtained as

$$\langle P_{abc}^i P_{def}^j \rangle_P = \sum_{\lambda_{ev}} \frac{1}{2} M_{\lambda_{ev}}^{ij} (a_{\lambda_{ev}} A + b_{\lambda_{ev}} B)_{abc,def}, \quad (81)$$

where $M_{\lambda_{ev}}^{ij}$ denotes the projector to the eigenspace of the eigenvalue λ_{ev} of Λ_{ij} .

Let us next start computing $\langle S_{eff}^{(4)}(P) \rangle_P$ by using the Wick contraction (81). Let us first compute the factors coming from the projectors. Let us restrict ourselves to the case $\Lambda_{ij} = \lambda + \lambda_d \delta_{ij}$, which is our interest as explained in Section 4. As given there, the eigenvector

for $\lambda_{ev} = \lambda R + \lambda_d$ is $(1, 1, \dots, 1)$, and those for $\lambda_{ev} = \lambda_d$ are the vectors transverse to that. Therefore the projectors are $M_{\lambda R + \lambda_d}^{ij} = 1/R$ for $\lambda_{ev} = \lambda R + \lambda_d$, and $M_{\lambda_d}^{ij} = \delta_{ij} - 1/R$ for $\lambda_{ev} = \lambda_d$, respectively. For later usage, let us compute the projectors sandwiched between $\tilde{\Lambda}_{ij}$:

$$(\tilde{\Lambda} M_{\lambda_{ev}} \tilde{\Lambda})_{ij} := \sum_{k,l=1}^R \tilde{\Lambda}_{ik} M_{\lambda_{ev}}^{kl} \tilde{\Lambda}_{lj} = \begin{cases} \lambda + \frac{\lambda_d}{R}, & \text{for } \lambda_{ev} = \lambda R + \lambda_d, \\ \lambda_d \delta_{ij} - \frac{\lambda_d}{R}, & \text{for } \lambda_{ev} = \lambda_d, \end{cases} \quad (82)$$

where we have used the following explicit solution to (22) for $\Lambda_{ij} = \lambda + \lambda_d \delta_{ij}$:

$$\tilde{\Lambda}_{ij} = p \delta_{ij} + q \text{ with } p^2 = \lambda_d, \quad 2pq + Rq^2 = \lambda. \quad (83)$$

As for the factor coming from the $\tilde{\Lambda}_{ij}$ in (69), the Wick contractions (81) of P_{abc}^i will generate the factor $\sum_j (\tilde{\Lambda} M_{\lambda_{ev}} \tilde{\Lambda})_{jj} (\tilde{\Lambda} M_{\lambda'_{ev}} \tilde{\Lambda})_{jj}$. Thus, using (82), we obtain the following results for each case:

$$\sum_{j=1}^R (\tilde{\Lambda} M_{\lambda_{ev}} \tilde{\Lambda})_{jj} (\tilde{\Lambda} M_{\lambda'_{ev}} \tilde{\Lambda})_{jj} = \begin{cases} R \left(\lambda + \frac{\lambda_d}{R} \right)^2, & \text{for } \lambda_{ev} = \lambda'_{ev} = \lambda R + \lambda_d, \\ R \left(\frac{(R-1)\lambda_d}{R} \right)^2, & \text{for } \lambda_{ev} = \lambda'_{ev} = \lambda_d, \\ R \left(\lambda + \frac{\lambda_d}{R} \right) \frac{(R-1)\lambda_d}{R}, & \text{otherwise.} \end{cases} \quad (84)$$

It is easy to see that all the other diagrams in Figure 6 have the same factor.

As for the Wick contractions (81) of $\langle (P\phi^3)^2 \rangle_\phi^c$ in (68), there exist two cases. One is to take the contractions within each $\langle (P\phi^3)^2 \rangle_\phi^c$, or otherwise. The former case can be called the disconnected case, and the latter the connected case, based on their diagrammatic characters. From (32) and (81), the factors coming from the Λ_{ij} 's are obtained as

$$\begin{aligned} \sum_{i,j=1}^R (\Lambda M_{\lambda_{ev}})_{ii} (\Lambda M_{\lambda'_{ev}})_{jj} &= \lambda_{ev} \lambda'_{ev} \text{Tr}(M_{\lambda_{ev}}) \text{Tr}(M_{\lambda'_{ev}}) \\ &= \begin{cases} (\lambda R + \lambda_d)^2, & \text{for } \lambda_{ev} = \lambda'_{ev} = \lambda R + \lambda_d, \\ (R-1)^2 \lambda_d^2, & \text{for } \lambda_{ev} = \lambda'_{ev} = \lambda_d, \\ (\lambda R + \lambda_d)(R-1)\lambda_d, & \text{otherwise,} \end{cases} \end{aligned} \quad (85)$$

$$\begin{aligned} \sum_{i,j=1}^R (\Lambda M_{\lambda_{ev}})_{ij} (\Lambda M_{\lambda'_{ev}})_{ji} &= \lambda_{ev}^2 \text{Tr}(M_{\lambda_{ev}}) \delta_{\lambda_{ev} \lambda'_{ev}}, \\ &= \begin{cases} (\lambda R + \lambda_d)^2, & \text{for } \lambda_{ev} = \lambda'_{ev} = \lambda R + \lambda_d, \\ (R-1)\lambda_d^2, & \text{for } \lambda_{ev} = \lambda'_{ev} = \lambda_d, \\ 0, & \text{otherwise.} \end{cases} \end{aligned} \quad (86)$$

for the disconnected and the connected cases, respectively.

The last ingredient for the computation of $S_{eff}^{(4)}(P)$ is to take into account the lower index part of the Wick contraction (81). As can be seen in (81), in general, this is to insert $xA + yA\tilde{B}A$ with some x, y at the location of the Wick contraction (See Figure 8 for an example). Diagrammatically, this is to insert the diagrams in Figure 7 at the location of the Wick

contraction. This insertion generates many diagrams with a number of loops. The number of loops gives the degeneracy of each diagram in powers of N . The summation over all the diagrams is too many to do so by hand, so we performed this task by using Mathematica. We have obtained

$$G_1(x, y) = 6N(2 + N)(4 + N)(225x^2 + 90Nx^2 + 9N^2x^2 + 456xy + 174Nxy + 18N^2xy + 232y^2 + 84Ny^2 + 8N^2y^2) \quad (87)$$

for $\langle (P\phi^3)^4 \rangle_\phi^c$. As for $\langle (P\phi^3)^2 \rangle_\phi^c$, we have obtained

$$G_2(x, y) = N^2(2 + N)^2(4 + N)^2(x + y)^2, \quad (88)$$

$$G_3(x, y) = 2N(2 + N)(4 + N)(15x^2 + 24xy + 6Nxy + 8y^2 + 6Ny^2 + N^2y^2), \quad (89)$$

respectively, for the disconnected and connected cases.

Let us combine all the results above. By using (81), (84) and (87) and summing over all the possibilities of the eigenspaces of Λ_{ij} , we obtain

$$\langle \langle (P\phi^3)^4 \rangle_\phi^c \rangle_P = \frac{R}{2^2(2\beta)^6} G_1(x_1, y_1), \quad (90)$$

where

$$x_1 = \left(\lambda + \frac{\lambda_d}{R} \right) a_{\lambda R + \lambda_d} + \frac{(R - 1)\lambda_d}{R} a_{\lambda_d}, \quad (91)$$

$$y_1 = \frac{3}{N + 2} \left(\left(\lambda + \frac{\lambda_d}{R} \right) b_{\lambda R + \lambda_d} + \frac{(R - 1)\lambda_d}{R} b_{\lambda_d} \right). \quad (92)$$

For the disconnected case of $\langle \langle (P\phi^3)^2 \rangle_\phi^c \rangle_P$, from (81), (85) and (88) we obtain

$$\langle \langle (P\phi^3)^2 \rangle_\phi^c \rangle_P^{discon} = \frac{1}{2^2(2\beta)^6} G_2(x_2, y_2), \quad (93)$$

where

$$x_2 = (\lambda R + \lambda_d) a_{\lambda R + \lambda_d} + (R - 1)\lambda_d a_{\lambda_d}, \quad (94)$$

$$y_2 = \frac{3}{N + 2} ((\lambda R + \lambda_d) b_{\lambda R + \lambda_d} + (R - 1)\lambda_d b_{\lambda_d}). \quad (95)$$

For the connected part of $\langle \langle (P\phi^3)^2 \rangle_\phi^c \rangle_P$, from (81), (86) and (89) we obtain

$$\langle \langle (P\phi^3)^2 \rangle_\phi^c \rangle_P^{con} = \frac{1}{2^2(2\beta)^6} ((\lambda R + \lambda_d)^2 G_3(x_3, y_3) + (R - 1)\lambda_d^2 G_3(x_4, y_4)), \quad (96)$$

where

$$(x_3, y_3) = \left(a_{\lambda R + \lambda_d}, \frac{3b_{\lambda R + \lambda_d}}{N + 2} \right), \quad (97)$$

$$(x_4, y_4) = \left(a_{\lambda_d}, \frac{3b_{\lambda_d}}{N + 2} \right).$$

By putting (90), (93) and (96) into (68), we obtain the final result given in (41) and (42).

D Brief introduction of persistent homology

In this appendix, we give a brief introduction of persistent homology for this paper to be self-contained. More details can be found for instance in [30].

Persistent homology is a notion that characterizes the topological aspect of a data in terms of homology. A data to be analyzed is supposed to be a set of points with relative distances. From the data, a stream (or a filtration) of simplicial complexes parameterized by a scale parameter, say u , is constructed. Roughly speaking, the scale u parameterizes the resolution of topological structure of interest. In other words, persistent homology characterizes a data with multi-scale homologies. The details of the construction of a stream is given at the end of this appendix. Once a stream is constructed, the homology groups of the simplicial complexes at each value of u are computed. By increasing the value of u from zero, a homology group element will appear at a certain value of u , say u_{start} , and will disappear at another value, say u_{end} . If $u_{\text{end}} - u_{\text{start}}$ is large, one may regard the element as a persistent homology group element, which has a long life. The collection of persistent homology group elements characterizes the topological property of a data set. There will also be a number of short-life elements, but they are often regarded as “noises”, which are not robust against small perturbations of the data.

There are two kinds of diagrams that are convenient for visualizing the persistent homology of a data. One is called barcode diagram, where each horizontal line represents a homology group element that exists during the period of u indicated by a line segment. An example of barcode diagrams from the actual data of our Monte Carlo simulation is shown in Figure 9. The left figure shows the barcode diagram for the 0-dimensional homology, and the right that for the 1-dimensional homology. The left diagram indicates that the initially separated points form one connected component over the scale $u \sim 1.4$. The right figure shows that there exists a one-dimensional cycle which has the large size of $u \sim 1.8$, while there is a small “noise” around $u \sim 0.9$. In Figure 10, we provide the graph constructed by connecting the points with relative distances smaller than 1.5, using the same data used for Figure 9. One can actually see the presence of a one-dimensional cycle consistent with the bar code diagram.

The other kind of diagram is called persistent diagram. An element that is represented by a line segment $[u_{\text{start}}, u_{\text{end}}]$ in a barcode diagram is represented by a dot located at the two-dimensional coordinate $(u_{\text{start}}, u_{\text{end}})$ in a persistent diagram. Since there are multiple elements in general, and $u_{\text{start}} < u_{\text{end}}$, a persistent diagram contains a number of dots in the region over the diagonal line. The long-life elements are represented by the dots that exist away from the diagonal line, and those in the vicinity of the diagonal line are regarded as “noises”. An example of a persistent diagram is given in Figure 11, which corresponds to the right barcode diagram in Figure 9. What is convenient in a persistent diagram is that one can easily superimpose persistent diagrams from multiple data. If there is a common characteristics through multiple data, one can find it as a characteristic pattern in a superimposed persistent diagram. Therefore, we use persistent diagrams to find statistically favored structure common in the configurations generated by the Monte Carlo simulation.

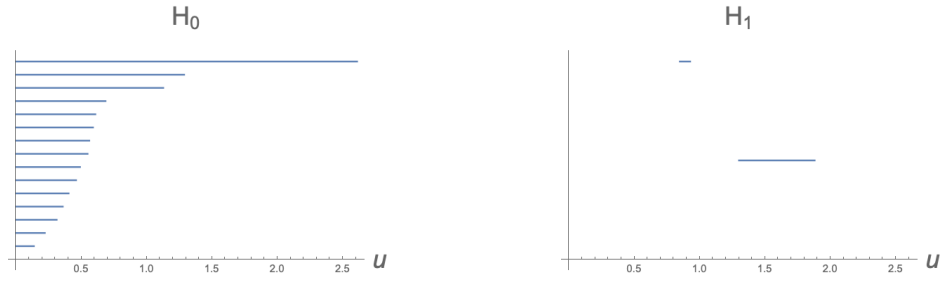


Figure 9: An example of barcode diagrams. The example is obtained by analyzing a configuration ϕ_a^i ($i = 1, 2, \dots, R$) generated by the actual Monte Carlo simulation for $N = 4$, $R = 15$, and $k = 0.01$. The presence of a long-life one-dimensional homology group element can be observed in this particular data.

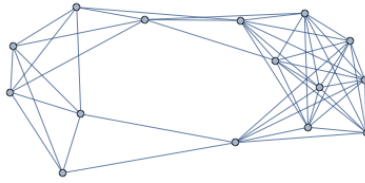


Figure 10: A graph made by connecting the points with relative distances smaller than 1.5. The data is the same one used for Figure 9. This choice of the distance cut-off is made because a one-dimensional cycle is expected to exist at this scale, seeing the right of Figure 9.

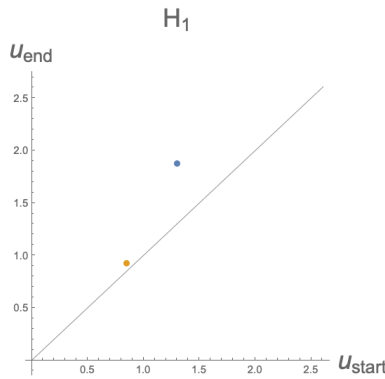


Figure 11: The persistent diagram corresponding to the right barcode diagram in Figure 9. A line segment in a barcode diagram is represented by a dot in a persistent diagram. The longest one is represented by a blue dot, and the second by a yellow one. This usage of colors is also done in Section 7.

Let us finally explain the actual construction of a stream of simplicial complexes parameterized by u . In fact, there exist various streams depending on purposes in the literature, but let us restrict ourselves to the Vietoris-Rips stream, which is used in the open-source c++ code called Ripser. For a given data that stores distances between points, the Vietoris-Rips stream $\text{VR}(V, u)$ is defined as follows:

- The vertex set is given by the point set V of a data.
- For vertices i and j with distance $d(i, j)$, the edge $[i, j]$ are included in $\text{VR}(V, u)$, if and only if $d(i, j) \leq u$.
- A higher-dimensional simplex is included in $\text{VR}(V, u)$, if and only if all of its edges are.

From the above definition, there is an obvious property, $\text{VR}(V, u) \subset \text{VR}(V, u')$ for $u < u'$. An important fact is that this induces a map: $H_k(\text{VR}(V, u)) \rightarrow H_k(\text{VR}(V, u'))$ for $u < u'$. Therefore, the development of each homology group element under the change of the value of u can be followed, and its life is characterized by the two endpoint values of u . This makes barcode and persistent diagrams convenient ways for the description.

References

- [1] M. Reuter and F. Saueressig, “Quantum Gravity and the Functional Renormalization Group : The Road towards Asymptotic Safety,” Cambridge University Press, 2019.
- [2] R. Loll, “Quantum Gravity from Causal Dynamical Triangulations: A Review,” arXiv:1905.08669 [hep-th].
- [3] C. Rovelli and F. Vidotto, “Covariant Loop Quantum Gravity : An Elementary Introduction to Quantum Gravity and Spinfoam Theory,” Cambridge University Press, 2014.
- [4] S. Surya, “The causal set approach to quantum gravity,” arXiv:1903.11544 [gr-qc].
- [5] T. Konopka, F. Markopoulou and L. Smolin, “Quantum Graphity,” hep-th/0611197.
- [6] E. Wigner, “Characteristic vectors of bordered matrices with infinite dimensions”, *Annals of Mathematics* **62** (3): 548-564.
- [7] G. 't Hooft, “A planar diagram theory for strong interactions,” *Nucl. Phys. B* **72**, 461 (1974).
- [8] E. Brezin and V. A. Kazakov, “Exactly Solvable Field Theories of Closed Strings,” *Phys. Lett. B* **236**, 144 (1990). doi:10.1016/0370-2693(90)90818-Q
- [9] M. R. Douglas and S. H. Shenker, “Strings in Less Than One-Dimension,” *Nucl. Phys. B* **335**, 635 (1990). doi:10.1016/0550-3213(90)90522-F

- [10] D. J. Gross and A. A. Migdal, “Nonperturbative Two-Dimensional Quantum Gravity,” *Phys. Rev. Lett.* **64**, 127 (1990). doi:10.1103/PhysRevLett.64.127
- [11] J. Ambjorn, B. Durhuus, and T. Jonsson, “Three-dimensional simplicial quantum gravity and generalized matrix models,” *Mod. Phys. Lett.* **A06** (1991) 1133–1146.
- [12] N. Sasakura, “Tensor model for gravity and orientability of manifold,” *Mod. Phys. Lett.* **A06** (1991) 2613–2624.
- [13] N. Godfrey and M. Gross, “Simplicial quantum gravity in more than two-dimensions,” *Phys. Rev.* **D43** (1991) R1749–1753.
- [14] R. Gurau, “Colored Group Field Theory,” *Commun. Math. Phys.* **304**, 69 (2011) doi:10.1007/s00220-011-1226-9 [arXiv:0907.2582 [hep-th]].
- [15] G. Narain, N. Sasakura and Y. Sato, “Physical states in the canonical tensor model from the perspective of random tensor networks,” *JHEP* **1501**, 010 (2015) doi:10.1007/JHEP01(2015)010 [arXiv:1410.2683 [hep-th]].
- [16] N. Sasakura, “Canonical tensor models with local time,” *Int. J. Mod. Phys. A* **27**, 1250020 (2012) doi:10.1142/S0217751X12500200 [arXiv:1111.2790 [hep-th]].
- [17] N. Sasakura, “Uniqueness of canonical tensor model with local time,” *Int. J. Mod. Phys. A* **27**, 1250096 (2012) doi:10.1142/S0217751X12500960 [arXiv:1203.0421 [hep-th]].
- [18] D. Obster and N. Sasakura, “Emergent symmetries in the canonical tensor model,” *PTEP* **2018**, no. 4, 043A01 (2018) doi:10.1093/ptep/pty038 [arXiv:1710.07449 [hep-th]].
- [19] T. Kawano, D. Obster and N. Sasakura, “Canonical tensor model through data analysis: Dimensions, topologies, and geometries,” *Phys. Rev. D* **97**, no. 12, 124061 (2018) doi:10.1103/PhysRevD.97.124061 [arXiv:1805.04800 [hep-th]].
- [20] D. Obster and N. Sasakura, “Symmetric configurations highlighted by collective quantum coherence,” *Eur. Phys. J. C* **77**, no. 11, 783 (2017) doi:10.1140/epjc/s10052-017-5355-y [arXiv:1704.02113 [hep-th]].
- [21] L. Lionni and N. Sasakura, “A random matrix model with non-pairwise contracted indices,” *PTEP* **2019**, no. 7, 073A01 (2019) doi:10.1093/ptep/ptz057 [arXiv:1903.05944 [hep-th]].
- [22] A. Anderson, R. C. Myers and V. Periwal, “Complex random surfaces,” *Phys. Lett. B* **254**, 89 (1991).
- [23] A. Anderson, R. C. Myers and V. Periwal, “Branched polymers from a double scaling limit of matrix models,” *Nucl. Phys. B* **360**, 463 (1991).
- [24] R. C. Myers and V. Periwal, “From polymers to quantum gravity: Triple scaling in rectangular random matrix models,” *Nucl. Phys. B* **390**, 716 (1993) [hep-th/9112037].

- [25] S. Nishigaki and T. Yoneya, “A nonperturbative theory of randomly branching chains,” Nucl. Phys. B **348**, 787 (1991). doi:10.1016/0550-3213(91)90215-J
- [26] P. Di Vecchia, M. Kato and N. Ohta, “Double scaling limit in $O(N)$ vector models in D -dimensions,” Int. J. Mod. Phys. A **7**, 1391 (1992). doi:10.1142/S0217751X92000612
- [27] A. Crisanti and H.-J. Sommers, “The spherical p -spin interaction spin glass model: the statics,” Z. Phys. B **87**, 341 (1992).
- [28] T. Castellani and A. Cavagna, “Spin-glass theory for pedestrians”, J. Stat. Mech.: Theo. Exp. **2005**, 05012 [arXiv: cond-mat/0505032].
- [29] N. Sasakura, “Quantum canonical tensor model and an exact wave function,” Int. J. Mod. Phys. A **28**, 1350111 (2013) doi:10.1142/S0217751X1350111X [arXiv:1305.6389 [hep-th]].
- [30] G. Carlsson, “Topology and data,” Bulletin of the American Mathematical Society, **46**(2), 255-308, DOI: 10.1090/S0273-0979-09-01249-X.